



An investigation of C, N, and Na abundances in red giant stars of the Sculptor dwarf spheroidal galaxy

C. Salgado,[★] G. S. Da Costa[Ⓡ], J. E. Norris and D. Yong

Research School of Astronomy and Astrophysics, Australian National University, Canberra, ACT 2611, Australia

Accepted 2019 January 8. Received 2019 January 7; in original form 2018 September 10

ABSTRACT

The origin of the star-to-star abundance variations found for the light elements in Galactic globular clusters (GGCs) is not well understood, which is a significant problem for stellar astrophysics. While the light element abundance variations are very common in globular clusters, they are comparatively rare in the Galactic halo field population. However, little is known regarding the occurrence of the abundance anomalies in other environments such as that of dwarf spheroidal (dSph) galaxies. Consequently, we have investigated the anticorrelation and bimodality of CH- and CN-band strengths, which are markers of the abundance variations in GGCs, in the spectra of red giants in the Sculptor dwarf spheroidal galaxy. Using spectra at the Na D lines, informed by similar spectra for five GGCs (NGC 288, 1851, 6752, 6809, and 7099), we have also searched for any correlation between CN and Na in the Sculptor red giant sample. Our results indicate that variations analogous to those seen in GGCs are not present in our Sculptor sample. Instead, we find a weak positive correlation between CH and CN and no correlation between Na and CN. We also reveal a deficiency in [Na/Fe] for the Sculptor stars relative to the values in GGCs, a result that is consistent with the previous work for dSph galaxies. The outcomes reinforce the apparent need for a high stellar density environment to produce the light element abundance variations.

Key words: galaxies: abundances – galaxies: dwarf – galaxies: individual: (Sculptor dwarf spheroidal) – Galaxy: abundances.

1 INTRODUCTION

The study of Galactic globular clusters (GGCs) allows the investigation of many aspects of stellar evolution, and of the dynamics and chemical conditions at the moment when the host galaxy formed. However, detailed photometric and spectroscopic studies have demonstrated that GGCs possess a much more complex star formation history than previously thought. One of the main unsolved problems is the origin of the star-to-star abundance variation in the light elements (C, N, O, Na, Mg, and Al) and in helium that is seen in most, if not all, globular clusters. While approximately half of the stars in a typical cluster have abundance patterns similar to halo field stars, the other half of the stars in the cluster are depleted in carbon, oxygen, and magnesium, and enhanced in nitrogen, sodium, aluminium (e.g. Osborn 1971; Norris et al. 1981; Kraft 1994a; Gratton et al. 2001a; Gratton, Sneden & Carretta 2004; Salaris et al. 2006). While the evidence for the light element abundance variations is provided, inter alia, directly by spectroscopic determinations, the evidence for helium abundance variations comes primarily from

the existence of split or multiple main sequences (MS) observed in high-precision *HST*-based colour-magnitude diagrams (e.g. NGC 6752; Milone et al. 2013), and from interpretations of horizontal branch morphologies (e.g. D’Antona et al. 2005), though direct spectroscopic evidence does exist (e.g. Marino et al. 2014). See also Milone et al. (2018).

The effects of H-burning at high temperatures provide a clue to the origin of the observed abundance variations, as the abundances of light elements can be altered by the simultaneous action of p-capture reactions in the CNO, NeNa, and MgAl chains (Denisenkov & Denisenkova 1989; Langer, Hoffman & Sneden 1993; Prantzos, Charbonnel & Iliadis 2007). The temperatures required for these processes to occur are $\geq 20 \times 10^6$ K for the NeNa cycle and $\geq 70 \times 10^6$ K for the MgAl cycle. However, such temperatures are not reached in the interior of current GGC stars requiring the anomalies to come from an earlier generation or generations of stars. In order to explain these light element abundance variations, several types of stars have been proposed as possible polluters. The most popular are intermediate-mass asymptotic giant branch (AGB) stars (Cottrell & Da Costa 1981; D’Antona, Gratton & Chieffi 1983; Ventura et al. 2001) and/or super-AGB stars (Pumo, Siess & Zappala 2008; Ventura & D’Antona 2011; D’Antona et al.

* E-mail: carolina.salgado@anu.edu.au

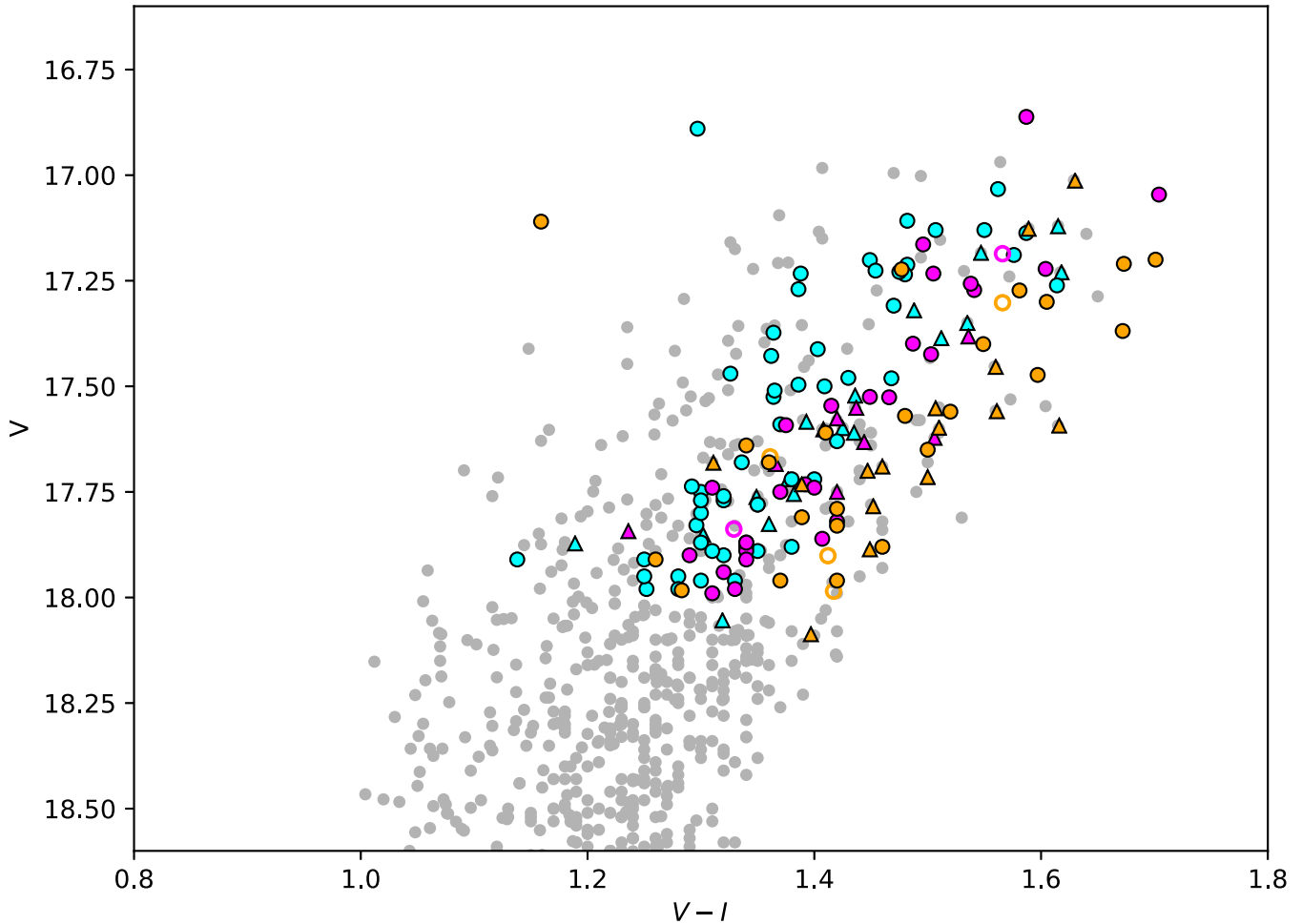


Figure 1. Position of the target stars in the Sculptor red giant branch CMD. The observed stars are shown as triangles for the 45 stars observed with GMOS-S and as circles for the remaining 108 stars with red spectra only. Open markers indicate the eight stars without a useable spectrum at the NaD lines while the grey small dots are for other Sculptor member stars from the studies of Walker et al. (2009a), Coleman et al. (2005), and Kirby et al. (2010). The photometry is taken solely from Coleman et al. (2005). For the observed stars the colour coding refers to different metallicity groups: cyan, magenta, and orange are used for stars with $[\text{Fe}/\text{H}] < -1.9$, $-1.9 \leq [\text{Fe}/\text{H}] \leq -1.6$, and $[\text{Fe}/\text{H}] > -1.6$, respectively.

Table 1. Details of the observations.

	Blue (GMOS-S) Sculptor	Blue (AAOmega) GGCs	Red (AAOmega) Sculptor and GGCs
Grating	B 1200	1700B	2000R
Resolution (\AA)	2.3	1.1	0.8
Observed stars	45	196	153 ^b –196 ^c
Central wavelength	4400 \AA and 4350 \AA ^a	4100 \AA	6050 \AA

Note. ^aObserved at two different central wavelengths.

^bUseful Sculptor spectra.

^cGlobular Cluster spectra. 164 GGC spectra were used after excluding AGB and low S/N spectra.

2016), supermassive stars (Denissenkov & Hartwick 2013) and fast rotating massive stars (FRMS) (Norris 2004; Maeder & Meynet 2006; Decressin et al. 2007, 2009). These stars allow a hot H-burning environment, a mechanism to bring the processed material to the surface (convection and rotational mixing for AGBs and FRMS, respectively), and a way to release this material into the intracluster medium at a velocity sufficiently low to avoid escaping from the cluster potential well. Renzini et al. (2015) test, discuss, and summarize several scenarios and reveal the successes and

deficiencies of each of them based on the evidence provided by the results of the *Hubble Space Telescope* (HST) UV Legacy Survey of GGCs (Piotto et al. 2015). See also Bastian & Lardo (2018).

The abundance anomalies have been found in all evolutionary phases of GGC stars from the MS to the giant branch. Specifically, the presence of abundance anomalies on the MS of several GGCs, for example NGC 104, NGC 288, NGC 6205, and NGC 6752 (e.g. Smith & Norris 1982; Sneden et al. 1994; Gratton et al. 2004; Lee, Carney & Balachandran 2004; Carretta et al. 2010), requires that

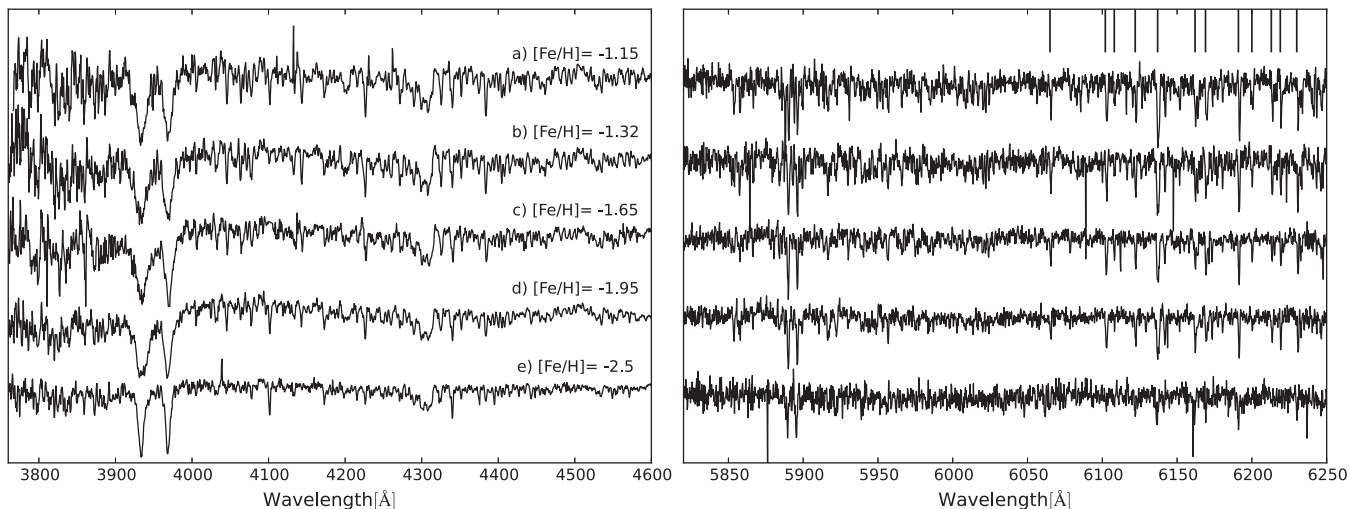


Figure 2. Examples of the continuum-normalized velocity-corrected spectra of Scl target stars at different metallicities. The spectra have been shifted vertically and the metallicity values are indicated. The left-hand panel shows GMOS-S Gemini blue spectra, while red spectra from AAOmega are shown in the right-hand panel. The colours and magnitudes of the stars are as follows: (a) Scl-0233: $V = 17.55$, $V - I = 1.50$; (b) Scl-0470: $V = 17.78$, $V - I = 1.45$; (c) Scl23: $V = 17.84$, $V - I = 1.23$; (d) Scl-0468: $V = 17.61$, $V - I = 1.43$; and (e) Scl-0272: $V = 17.58$, $V - I = 1.39$. The vertical lines in the upper portion of the right panel indicate the location of the spectral lines used to determine the metallicities.

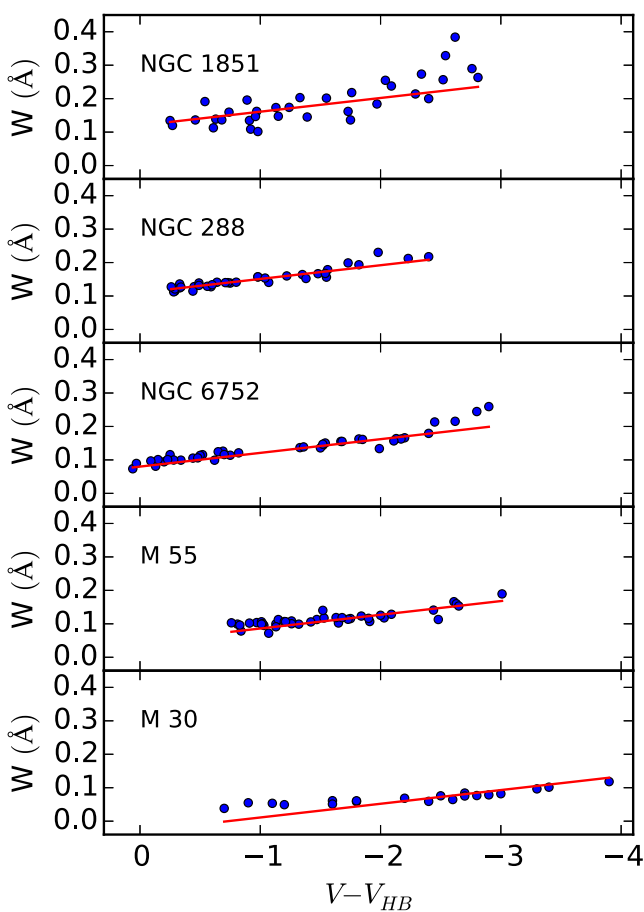


Figure 3. Plot of the equivalent width of the combined Ca, Fe, and Ni lines against $(V - V_{HB})$ for the five GGC calibration clusters. The clusters are ordered in decreasing metallicity from top to bottom. The red line is the mean slope, $\alpha = -0.04 \text{ \AA mag}^{-1}$.

Table 2. Adopted parameters from Harris (1996) catalogue.

GGC ID	[Fe/H]	V_{HB}	$(m - M)_V$	$E(B - V)$
M 30	-2.27	15.10	14.64	0.03
M 55	-1.94	14.40	13.89	0.08
NGC 6752	-1.54	13.70	13.13	0.04
NGC 288	-1.32	15.44	14.84	0.03
NGC 1851	-1.18	16.09	15.47	0.02

the anomalies come from a previous generation or generations. We note, however, that star-to-star variations in the heavy elements (e.g. Ca and Fe) are not common in GGCs, and are instead restricted to a small number of clusters such as ω Centauri, M22, and M54.

The study of chemical abundance patterns is not restricted to GGCs: for example, their study in individual metal-poor stars provides clues about element formation and evolution in the universe. In particular, carbon and nitrogen play a crucial role in understanding the evolution of galaxies because they are produced by different mechanisms and by stars of a wide range of mass. Many studies show that the strength of the CN molecular bands in the spectra of red giant stars is a good indicator of $[N/Fe]$ while the CH-band provides a measure of $[C/Fe]$ (e.g. Smith et al. 1996). Carbon and nitrogen have been studied in different environments. For example, in GGC red giants, spectroscopic studies of CN- and CH-band strengths have shown that there is generally an anticorrelation between CN- and CH-band strengths, coupled with a bimodality of CN-band strength that allows the classification of stars as CN-strong or CN-weak (e.g. Norris et al. 1981; Norris, Freeman & Da Costa 1984; Pancino et al. 2010). Spectrum synthesis calculations have demonstrated that these CN- and CH-band strength variations are a direct consequence of differences in C and N abundances, with C depleted and N enhanced in the so-called ‘second generation’ (CN-strong) stars as compared to the Galactic halo-like abundances in the ‘first generation’ (CN-weak) stars.

As regards dSph galaxies, Shetrone et al. (2013) analysed CN and CH molecular band strengths in the spectra of 35 red giants in the Draco dSph. They found little evidence for any spread in

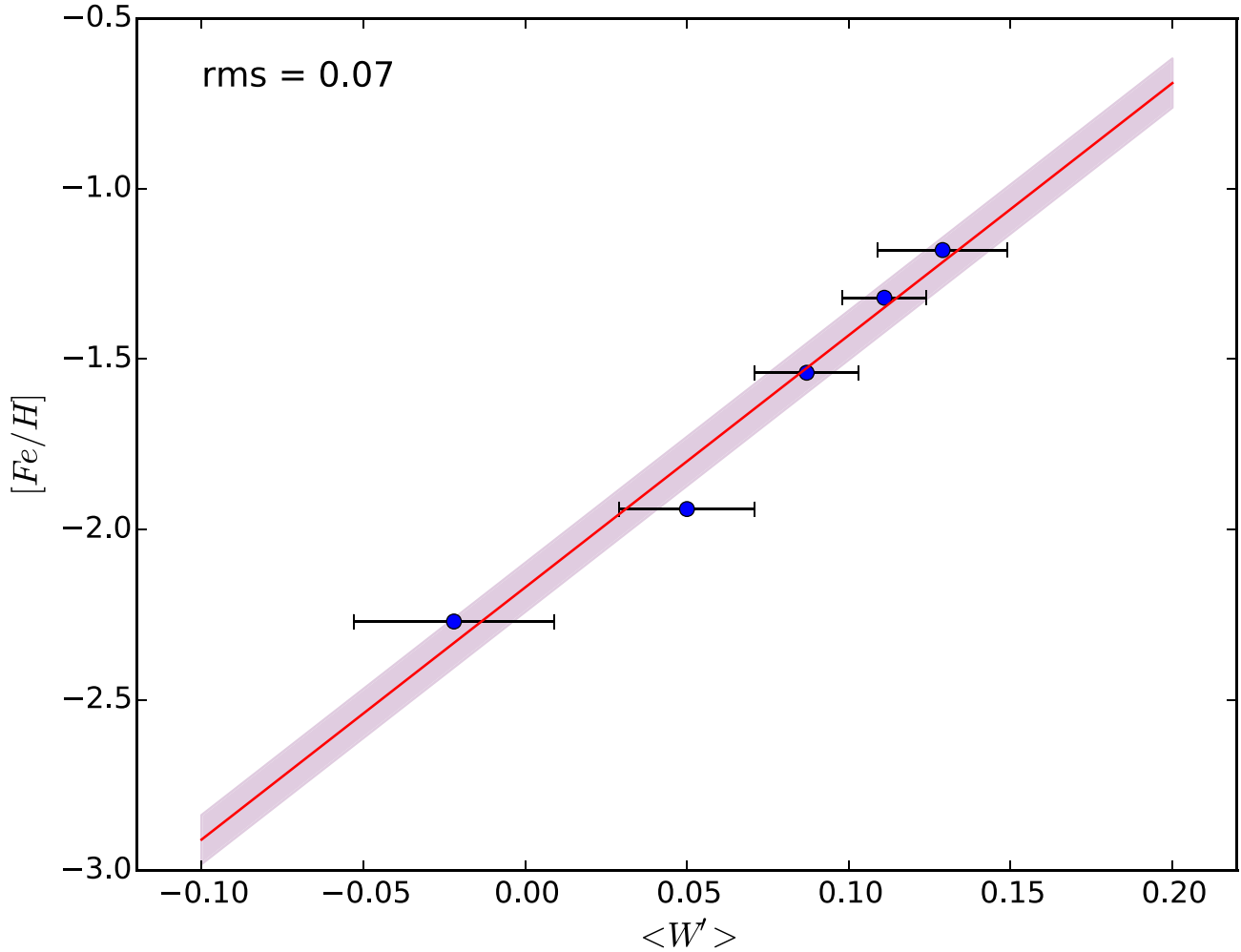


Figure 4. $[Fe/H]$ against $\langle W' \rangle$ for the five calibration globular clusters. The metallicities were taken from the most recent online version of the Harris (1996) catalogue (see Table 2). The red line is the best fit to the data and the shaded area is the rms dispersion. The error bars shown are the mean error calculated from the propagation of the uncertainties for each set of cluster W' values.

CN-band strength at a given luminosity, and, in contrast to the anticorrelation seen in GGCs, the CN- and CH-band strengths were found to be generally correlated. Using spectrum syntheses, they showed that the carbon abundances decrease with increasing luminosity consistent with the expectations of evolutionary mixing, a phenomenon that is also seen in field stars and globular clusters in the halo. Shetrone et al. (2013) also found evidence for an intrinsic spread in $[C/Fe]$ at fixed $[Fe/H]$ and/or M_{bol} in their sample, which they interpreted as having at least a partial primordial origin.

Kirby et al. (2015) also studied the carbon abundances of a large sample of red giant stars in both GGCs and dSphs seeking to understand the relation between the dSphs, the Galactic halo and their chemical enrichment. For non-carbon enhanced stars, i.e. those with $[C/Fe] \leq 0.7$, Kirby et al. (2015) compared the trend of $[C/Fe]$ versus $[Fe/H]$ for dSphs with the trend for Galactic halo stars, finding that the ‘knee’ in $[C/Fe]$ occurs at a lower metallicity in the dSphs than in the Galactic halo. The knee corresponds to the metallicity at which SNe Ia begin to contribute to the chemical evolution, and the difference in the location of the knee caused Kirby et al. (2015) to suggest that SNe Ia activity is more important at lower metallicities in dSphs than it is in the halo.

In a similar fashion, Lardo et al. (2016) reported the results of a study of carbon and nitrogen abundance ratios, obtained from CH and CN index measurements, for 94 red giant branch (RGB) stars in the Sculptor (Scl) dSph. The results indicate that $[C/Fe]$ decreases with increasing luminosity across the full metallicity range on the Scl red giant branch. More specifically, the measurements of $[C/Fe]$ and $[N/Fe]$ are in excellent agreement with theoretical model predictions (Stancliffe et al. 2009) that show the red giants experience a significant depletion of carbon after the first dredge-up. Lardo et al. (2016) also reported the discovery of two carbon-enhanced metal-poor (CEMP) stars in Scl, both of which show an excess of barium consistent with s-process nucleosynthesis.

Studies of carbon abundances have also been made in ultra-faint dwarf galaxies: for example, Norris et al. (2010) present carbon abundances for red giant stars in the Boötes I and Segue 1 systems. They show that the stars in these ultra-faint dwarf galaxies that have $[Fe/H] \leq -3.0$ exhibit a relation between $[C/Fe]$ and $[Fe/H]$ similar to that seen for Galactic halo stars. Further, Norris et al. (2010) also found a carbon-rich and extremely metal-poor star ($[C/Fe] = +2.3$, $[Fe/H] = -3.5$) in Segue 1 that is similar to the CEMP stars found in the Galactic halo.

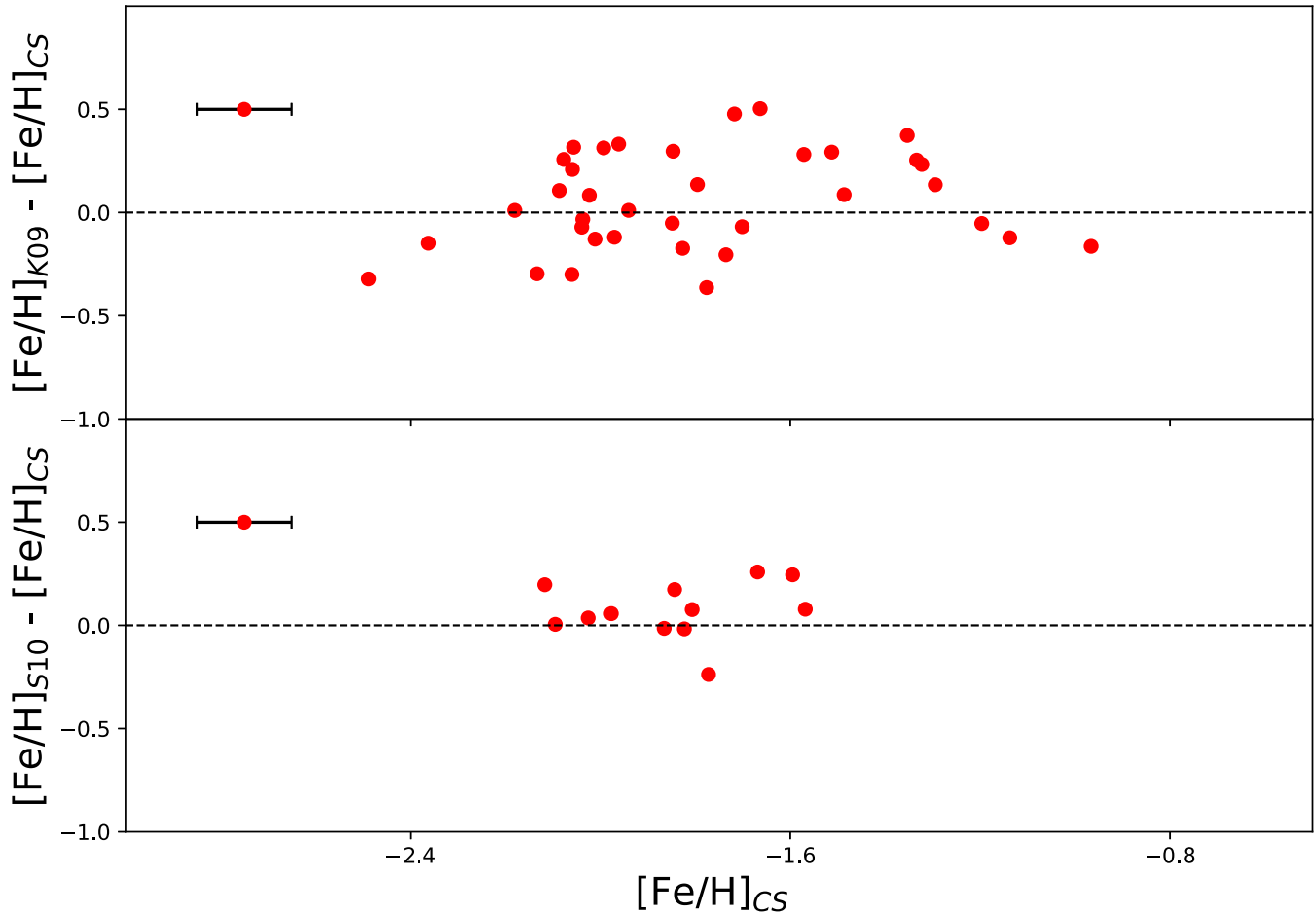


Figure 5. Estimation of $[\text{Fe}/\text{H}]$ for Sculptor stars compared with literature values. The upper panel shows the difference between $[\text{Fe}/\text{H}]$ found in Kirby et al. (2009) and $[\text{Fe}/\text{H}]$ from the current calibration ($[\text{Fe}/\text{H}]_{CS}$) against $[\text{Fe}/\text{H}]_{CS}$. The lower panel shows the difference between Starkenburg et al. (2010) and $[\text{Fe}/\text{H}]_{CS}$ against $[\text{Fe}/\text{H}]_{CS}$. Error bars ($\pm 1\sigma$ with $\sigma = 0.1$ dex) for the $[\text{Fe}/\text{H}]_{CS}$ values are shown.

However, it is not possible to directly relate any of these findings to the GGCs abundance anomalies problem without information on the Na abundance in the stars: the GGC characteristic signature of Na-enhancement coupled with C-depletion and N-enhancement needs to be investigated to decide if the C-, N-variations in Scl and other dSphs are merely the result of evolutionary mixing on the RGB, or arise from other nucleosynthetic processes unrelated to that for the GGC abundance anomalies. A further signature of the abundance variations in GGCs is the anticorrelation between sodium and oxygen abundances, which is seen at all evolutionary phases including the MS (Gratton et al. 2001b). The large spread in Na and O in GGCs (e.g. Carretta et al. 2009; Carretta 2016) further emphasizes that GGCs are not simple stellar populations. This signature also results in a correlation between sodium abundances and CN-band strengths, in which CN-strong red giant stars (enhanced in N, depleted in C) are also enhanced in Na (Cottrell & Da Costa 1981; Norris & Pilachowski 1985).

In this context we note that Shetrone et al. (2003) have studied $[\text{Na}/\text{Fe}]$ values for small samples of red giants in the Carina, Sculptor, Fornax and Leo I dwarf spheroidal galaxies. The results show that the dSph stars have low $[\text{Na}/\text{Fe}]$ values compared to halo stars with similar $[\text{Fe}/\text{H}]$. Further, Geisler et al. (2005) measured $[\text{Na}/\text{Fe}]$ for a small number of red giants in Sculptor and found a similar result: the dSph stars were deficient in $[\text{Na}/\text{Fe}]$ compared

to ‘first-generation’ GGC and Galactic halo field stars. Letarte et al. (2010) and Lemasle et al. (2014) have shown that this is also the case in the Fornax dSph. However, in contrast, Aoki et al. (2009) found $[\text{Na}/\text{Fe}] \sim 0.0$ for five stars in Sextans dSph galaxy, although they also found one star with a very low abundance of sodium: $[\text{Na}/\text{Fe}] \sim -0.7$. Norris et al. (2017) studied the chemical enrichment of the Carina dSph via an abundance study of 63 RGB stars. They showed that the Carina stars also have lower $[\text{Na}/\text{Fe}]$ compared to GGC red giants, and most significantly in the current context, they found no strong evidence in the Carina stars for the Na–O anticorrelation present in GGCs (Norris et al. 2017).

As regards the presence of GGC abundance anomalies in the halo field, Martell et al. (2011) present results from spectra of 561 halo red giants. They searched for the anticorrelated CN- and CH-band strength behaviour seen in GGCs red giants, but found that just ~ 3 per cent of the sample exhibited band strengths similar to those of second-generation GGC stars. These halo field stars could be second-generation globular cluster stars that have either escaped from their parent cluster or originated in now disrupted GGCs. Using theoretical models of globular cluster formation with two generations of stars, Martell et al. (2011) interpreted their results as suggesting that escape from, and dissolution of, globular clusters could contribute significantly to the stellar population of the Galactic halo; their estimate is approximately ~ 17 per cent of the currently

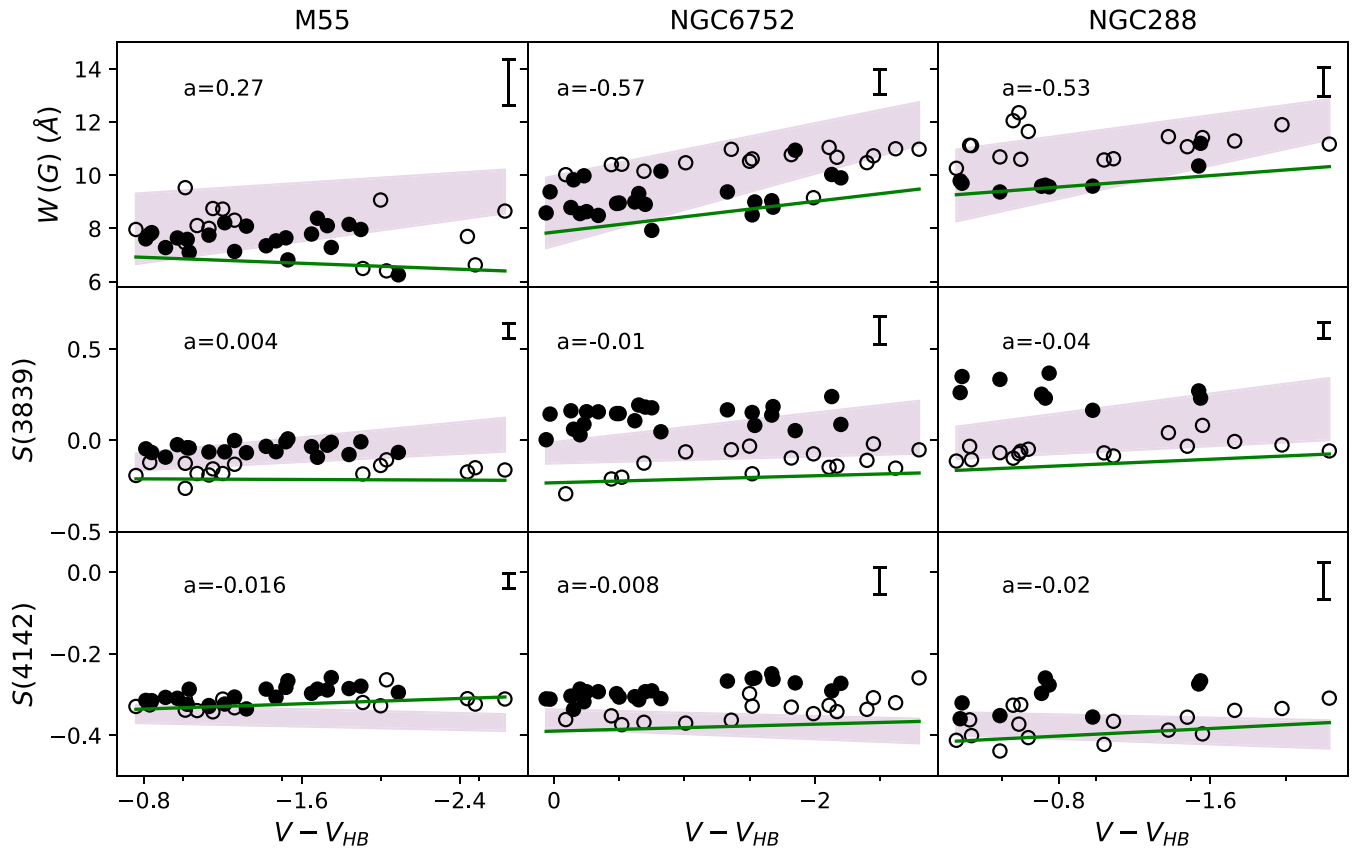


Figure 6. Dependence of the band-strength indices $W(G)$, $S(3839)$, and $S(4142)$ on $V - V_{HB}$ for RGB members of the GGCs M55, NGC 6752, and NGC 288. The central row is used to define CN-strong and CN-weak stars, which are represented by filled and open circles, respectively. The green straight lines are the adopted lower envelopes to the data for each index and cluster, and the corresponding slope values ‘ a ’ are given on the panels. The measurement error associated with each index and cluster is plotted in the top right corner of each panel. The error bars shown are $\pm 1\sigma$ in length. The shaded area in each panel is explained in Section 4.1.4.

mass of the stellar halo originated in this way. Similarly, Schiavon et al. (2016a) report the discovery in the APOGEE survey (Majewski 2016) of a population field stars in the inner Galaxy with high $[N/Fe]$ that is correlated with $[Al/Fe]$ and anticorrelated with $[C/Fe]$ in a similar fashion to that for the second-generation population in GGCs. If these stars have an origin as former members of disrupted GGCs then the total mass of such clusters must substantially exceed that of the surviving GGC system (Schiavon et al. 2016a), although the numbers may also indicate that the stars have a separate origin to that of the GGC stars (Schiavon et al. 2016a).

The aim of this work was to investigate if the abundance variations of the light elements seen in globular clusters are also present among the stars of the Sculptor dwarf spheroidal galaxy, in order to help constrain the origin of the anomalies. Sculptor is a well-studied dSph satellite galaxy of the Milky Way. It has $M_V \approx -11.2$, is strongly dominated by dark matter (Walker et al. 2007), and lies at a distance of 86 ± 5 kpc (Pietrzyński et al. 2008) from the Sun. The stellar population of Scl is dominated by old (age > 10 Gyr) metal-poor stars, and no significant star formation has occurred in the system for at least ≈ 6 Gyr (De Boer et al. 2012). In this paper we investigate the strengths of the CN and CH bands in the spectra of Sculptor red giants in order to test if the anticorrelation and bimodality seen in GGCs are also present in Sculptor. As an additional constraint, we have also estimated sodium abundances and explored the extent of any Na/CN correlation similar to that seen in the GGCs.

Our paper is arranged as follows. In Section 2 we present the observations, data reduction, and definition of the indices and their measurement; in Section 3 we outline our analysis procedure to derive overall metallicities; in Section 4 we present and discuss the results; and in Section 5 we summarize our findings and present our conclusions.

2 OBSERVATIONS AND DATA REDUCTION

Our input data set consists of 161 Sculptor red giant stars that have been identified as Scl members by Walker, Mateo & Olszewski (2009a), Coleman, Da Costa & Bland-Hawthorn (2005), and Battaglia et al. (2008). There are 114 stars brighter than $V = 17.8$ and 47 stars with magnitudes $17.8 < V \leq 18.1$. The position of the targets on the Scl RGB is presented in the CMD shown in Fig. 1. The full sample covers an area in excess of 1° in size, but the majority are found in a region $\sim 20'$ in diameter. The original intention was to observe the full sample with the Anglo-Australian Telescope (AAT) at Siding Spring Observatory using the 2dF multi-object fibre positioner and the AAOmega dual beam spectrograph (Saunders et al. 2004; Sharp et al. 2006). The spectrograph was configured with the 1700B grating in the blue arm, which provides a resolution of 1.1 \AA and the 2000R grating in the red arm, which provides a spectral resolution of 0.8 \AA . With this configuration, the observations cover the G band (CH, $\sim 4300 \text{ \AA}$) and the violet $\sim 3880 \text{ \AA}$ and blue $\sim 4215 \text{ \AA}$ CN bands in the blue spectra, and the NaD

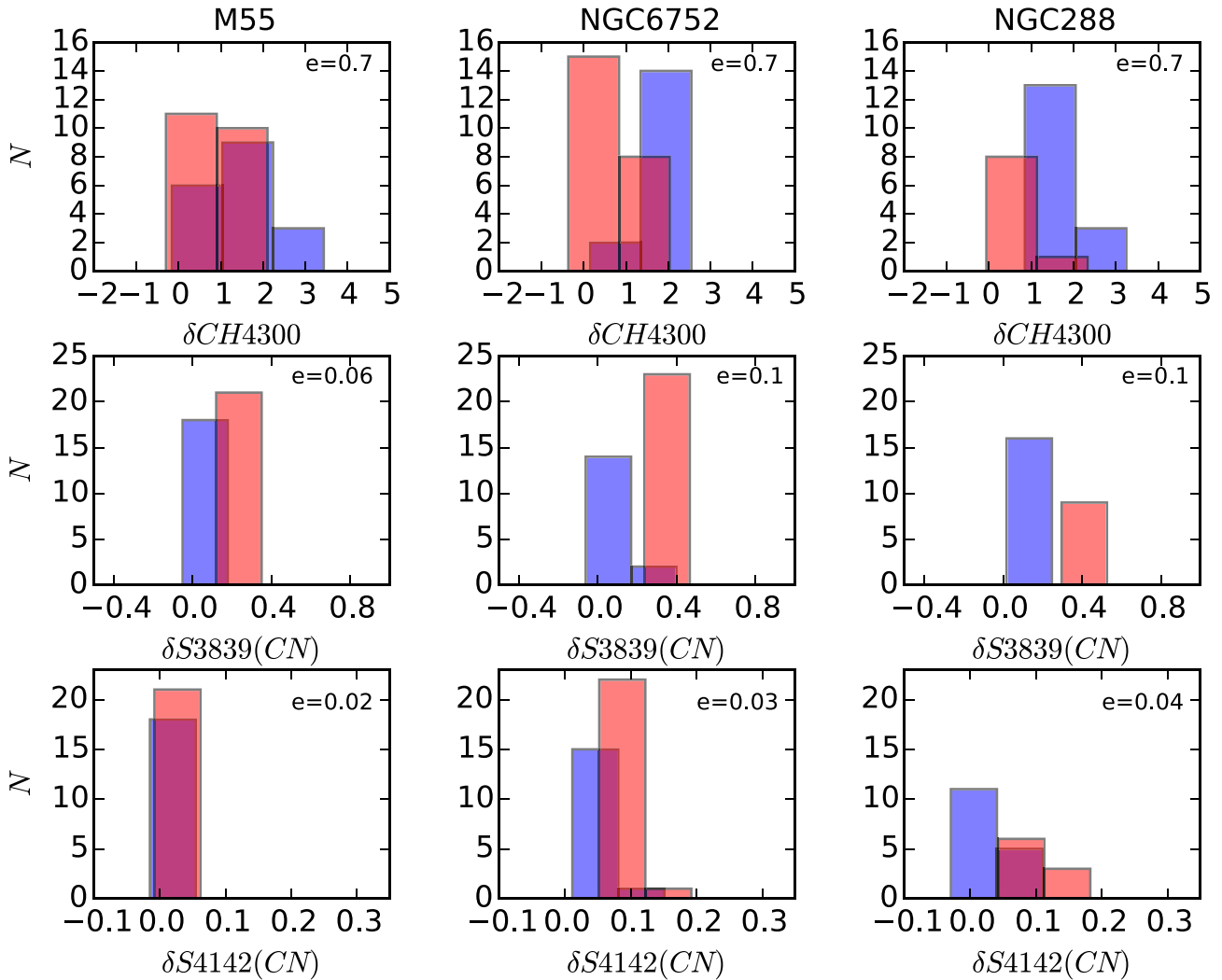


Figure 7. Histograms of $\delta W(G)$ (top row), $\delta S3839$ (middle row), and $\delta S4142$ (bottom row) for the GGC data. The cluster names are indicated at the top of the columns. The bin sizes chosen are slightly larger than the index errors, which are given in top right of each panel. CN-weak stars are shown in blue and CN-strong stars in red, with the classification coming from the middle row of Fig. 6.

lines in the red spectra whose coverage is approximately 5800–6255 Å.

Unfortunately, despite multiple night allocations across two successive observing seasons, the conditions did not permit usable blue spectra to be obtained for the Sculptor red giants. Nevertheless, good blue spectra were obtained for red giant stars in six globular clusters (M30, M55, NGC 2298, NGC 6752, NGC 288, and NGC 1851), and for Sculptor and GGCs red giants at the red wavelengths. The red spectra for the Sculptor stars consist of two distinct sets of combined multiple 1800 second exposures collected across three nights in 2011 October that resulted in 153 usable spectra at the NaD wavelengths. The red and blue spectra of the GGC stars were obtained in 2010 September and 2011 October. This data set consists of blue and red spectra for 196 stars belonging to the six GGCs, however, after the rejection of stars identified as likely AGB stars in photometric catalogues for the clusters, and removal of low signal-to-noise spectra, 164 GGC red giant spectra remain. Because of the lack of success with the AAT blue spectra, a subset of 45 Sculptor red giants was subsequently observed with the Gemini-South telescope (program GS-2012B-Q-5) and the Gemini Multi-Object Spectrograph (GMOS-S; Hook et al. 2004). The B1200

grating was used with 1 arcsec slits to yield a resolution of 2.3 Å. Six masks were observed with two integrations per mask at slightly different central wavelengths in order to compensate for the interchip gaps. The GMOS-S spectra were reduced, extracted and wavelength calibrated with standard IRAF/GEMINI software.¹ The red spectra for the Sculptor stars and the blue and red spectra for the GGC giants were reduced with the 2dF data reduction pipeline 2dfr.² Details of the observations are shown in Table 1.

In order to provide additional confirmation of the membership in the Sculptor dSph galaxy of the stars observed in this study, we have investigated the individual proper motions (μ_{RA} , μ_{Dec}) available from the Gaia DR2 data release (Gaia-Collaboration 2018). We find that all of the stars fall inside a circle centred on the mean values of μ_{RA} and μ_{Dec} with radius equal to 3σ , where σ is the standard deviation of the radial distances from the centre. We have

¹IRAF is distributed by the National Optical Astronomy Observatories, which are operated by the Association of Universities for Research in Astronomy, Inc., under cooperative agreement with the National Science Foundation.

²[HTTPS://WWW.AAO.GOV.AU/SCIENCE/SOFTWARE/2DFR](https://www.aao.gov.au/science/software/2dfr)

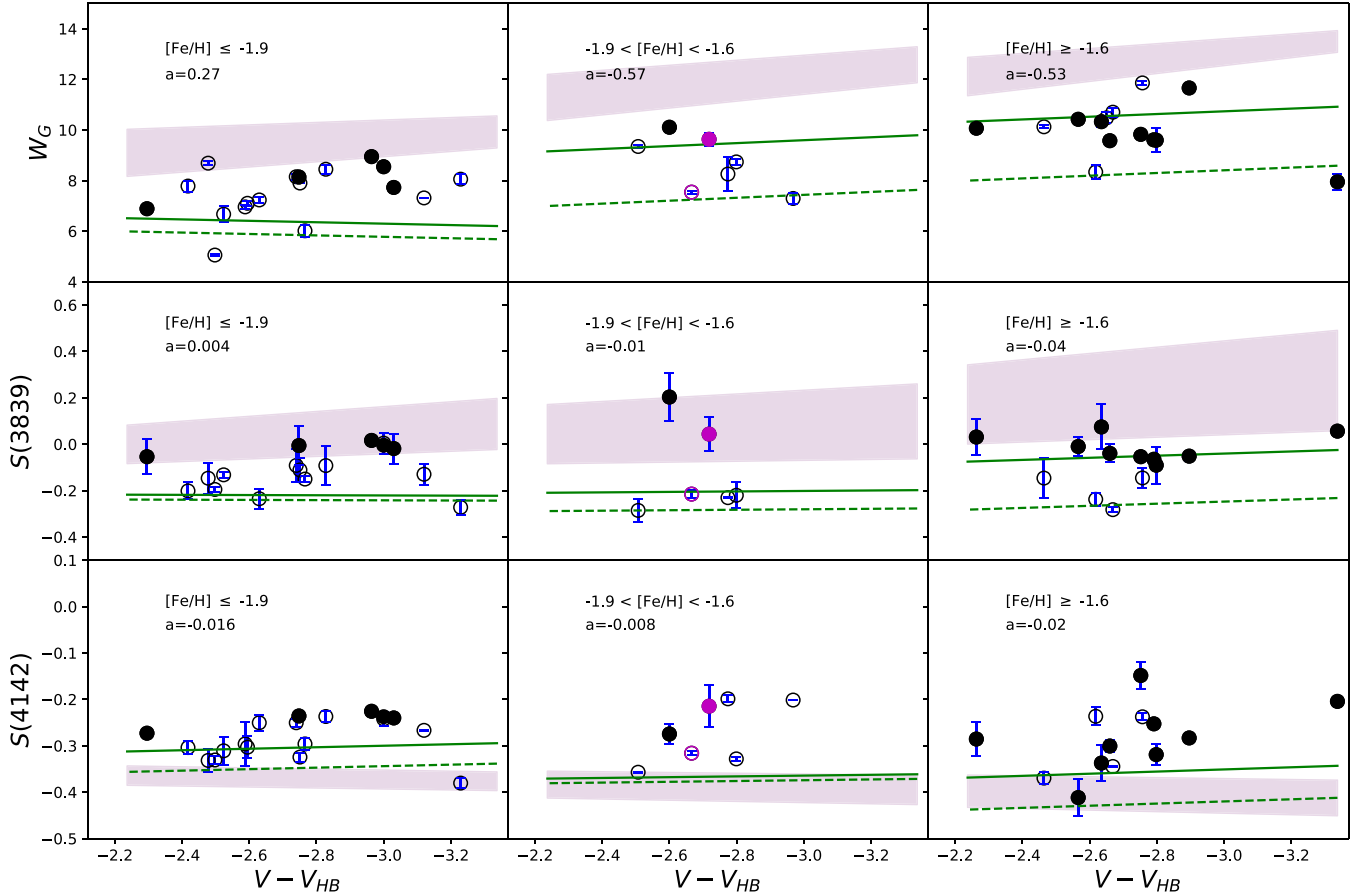


Figure 8. Dependence of the band-strength indices $W(G)$, $S(3839)$, and $S(4142)$ on $V - V_{HB}$ for the Scl stars, grouped into three metallicity ranges as indicated at the top of each panel. Stars characterized as CN-strong (from the $S(3839)$ index) are plotted as filled circles; open circles are CN-weak stars. The green dashed lines are the adopted lower envelopes to the Scl data. Their slopes (a), which are identical to those shown in Fig. 6, are shown. The green solid lines are the lower envelope lines from the GGC sample (Fig. 6) that have been extrapolated to higher luminosities when necessary. Individual uncertainties are shown for each star. The magenta open and filled circles (CN-weak and CN-strong, respectively) indicate stars Scl-0492 and Scl-0247, which are discussed in Section 4.2, and correspond to the stars in Fig. 13. The shaded area in each panel is explained in Section 4.1.4.

Table 3. Errors in $\delta W(G)$, $\delta S(3839)$, and $\delta S(4142)$ for the Scl stars.

Index	$-1.9 < [Fe/H] <$		
	$[Fe/H] \leq -1.9$	-1.6	$[Fe/H] \geq -1.6$
$\delta W(G)$	0.77	0.25	0.66
$\delta S(3839)$	0.05	0.07	0.04
$\delta S(4142)$	0.05	0.02	0.02

therefore no reason to doubt the Scl membership of any star in this sample.

2.1 Feature strengths

The analysis of CH and CN bands was based on the measurement via numerical integration of three indices that are sensitive to the strength of the bands in the spectra. In what follows F_λ is the intensity, and λ the wavelength, both from (pseudo-) continuum-normalized spectra. The spectra were (pseudo-) continuum-normalized by using standard IRAF routines: a low-order polynomial function was fit to the stellar (pseudo-) continua in order to consistently remove the overall shape of the spectra imposed by the convolution of the instrument response and the spectral energy distributions of the stars. The spectra were then shifted to rest

wavelength using the velocity derived from each observed spectrum. All subsequent analysis uses the (pseudo-) continuum-normalized, velocity-corrected spectra.

We first measured the strength of the $\lambda 3883 \text{ \AA}$ CN band by generating the index $S(3839)$ (Norris et al. 1981), which compares the intensity within the violet CN band with that of the nearby continuum.

$$S(3839) = -2.5 \log_{10} \left(\int_{3826}^{3883} F_\lambda d\lambda / \int_{3883}^{3916} F_\lambda d\lambda \right) \quad (1)$$

Second, we have measured the strength of the cyanogen band at $\lambda 4215 \text{ \AA}$ via the index $S(4142)$, which is explained in detail in Norris & Freeman (1979):

$$S(4142) = -2.5 \log_{10} \left(\int_{4120}^{4216} F_\lambda d\lambda / \int_{4216}^{4290} F_\lambda d\lambda \right) \quad (2)$$

Finally, we measured the strength of G band at $\sim 4300 \text{ \AA}$ by employing the $W(G)$ index given by Norris et al. (1984):

$$W(G) = \int_{4290}^{4318} (1 - F_\lambda / F_{4318}) d\lambda, \quad (3)$$

where F_{4318} comes from the mean of five maximal intensities in the range of wavelengths $\lambda \lambda 4314\text{--}4322 \text{ \AA}$.

As noted above, we employed the (pseudo-) continuum-normalized spectra for the band strength measurements; we have not attempted to flux-correct the spectra, a process that can be problematical for multifibre observations. Consequently, it is not possible to directly compare our band strength measurements with those made on flux-corrected spectra.

The CH and CN indices were measured on the Sculptor GMOS-S spectra, which have a resolution of 2.3 Å, and on the GGC AAOmega spectra that have a resolution of 1.1 Å. In order to check the effect of the different resolutions on the measurements, we smoothed the blue spectra of a selection of GGCs stars to match the resolution of the GMOS spectra, and remeasured the indices. We found that, on average, the difference for $S(3839)$ is only 0.01 mag (smaller at lower resolution). Similarly, we tested the effect of changing resolution on the $W(G)$ values. On average, the difference in $W(G)$ is ~ 1.3 Å, which, in the context of the average of $W(G)$ measurements, corresponds to ~ 13 per cent decrease at the lower resolution. We have not made any adjustments for this effect. Finally, the equivalent width (EW) of the Na D sodium absorption lines at ~ 5889 Å and ~ 5895 Å, were determined via Gaussian fits, using standard routines of IRAF, and the continuum-normalized velocity-corrected spectra. Examples of the blue (GMOS) and red (AAOmega) spectra for Sculptor stars with different metallicities are shown in Fig. 2.

3 METALLICITIES

Because Sculptor has a wide range of metallicities, we analysed the CH- and CN-band strengths for three distinct groups of Scl members: $[\text{Fe}/\text{H}] \leq -1.9$ (metal-poor stars), $-1.9 < [\text{Fe}/\text{H}] < -1.6$ (intermediate-metallicity stars), and $[\text{Fe}/\text{H}] \geq -1.6$ (metal-rich stars), as shown in Fig. 8. To determine the metallicities of the Sculptor stars, we followed an approach similar to that described in, e.g. Norris, Peterson & Hartwick (1983), Frebel et al. (2007), and Norris et al. (2012). In particular, we selected 12 strong lines of calcium, iron, and nickel in the RGB-star red spectra for use in the metallicity determination. The lines used are ~ 6102 Å, 6122 Å, 6162 Å, and 6169 Å for Ca I lines; ~ 6065 Å, 6137 Å, 6191 Å, 6200 Å, 6213 Å, 6219 Å, and 6230 Å for Fe I lines; and ~ 6108 Å for Ni I. A small region around each line was extracted from the continuum-normalized velocity-corrected spectra and the wavelength scale offset by the rest wavelength (in air) of the line, so that the line centre was at zero wavelength. The wavelength-offset regions for each line were then combined using standard IRAF routines to form a single-line profile. This process has the effect of increasing the signal-to-noise in the combined line profile facilitating the measurement, via fitting a Gaussian profile, of the equivalent width. The approach was applied to the red spectra of the GGC stars as well as to the red spectra of the Scl members.

In Fig. 3 we show the resulting EW values for the cluster stars plotted against $V - V_{\text{HB}}$, where the V_{HB} values were taken from the current online version of the Harris (1996) catalogue (see Table 2). For each cluster the line of best fit was calculated, and, since the slopes did not vary significantly from cluster to cluster, the average slope was determined and refit to the cluster values, as shown in Fig. 3. The slope is $\alpha = -0.04$ Å mag $^{-1}$ and the error in the slope is ± 0.013 , the standard error of the mean of the slope estimates for the five GGCs. The error in the slope will be propagated into the calculation of the reduced equivalent width (defined in the next paragraph). We note that the GGC NGC 2298 has not been considered in this calibration process because the small number of

stars in this cluster with sufficient S/N yielded a slope that was substantially different from that for the other clusters.

We then used α to set the reduced equivalent width W' for each star, with W' defined by $W' = (EW) - \alpha(V - V_{\text{HB}})$. The average reduced equivalent width for each GGC was then computed and plotted against the cluster metallicities from the current online version of the Harris (1996) catalogue (see Table 2). The error bars correspond to the mean error calculated from the propagation of the uncertainties in quadrature and then divided by the number of values for each set of cluster W' values. The result is shown in Fig. 4, together with a linear fit to the data points. The relation found is $[\text{Fe}/\text{H}] = 7.40 \pm 0.18 < W' > - 2.17 \pm 0.18$ and the rms dispersion about the fit is 0.07 dex. We then used this relation to compute the metallicity for each star in our Scl sample from the measured EW values and each star's $V - V_{\text{HB}}$ value, using a value of $V_{\text{HB}} = 20.35$ for Scl (Tolstoy et al. 2001). There are two sets of Scl spectra so the two EW measurements were averaged to determine the final value. The mean difference between the two sets of W' then enables us to estimate a typical metallicity error: the standard deviation of the differences is of order 0.01–0.015 Å (~ 10 –15 per cent of a typical EW value of 0.1 Å) and with the calibration this corresponds to a metallicity error of ~ 0.1 dex.

We have then compared our Scl metallicity values with the literature results of Kirby et al. (2009) and Starkenburg et al. (2010). First, our determination of the mean metallicity for Scl, based on the 146 stars for which we have a metallicity estimate, is $[\text{Fe}/\text{H}]_{\text{mean}} = -1.81$ dex. This value is entirely consistent with the mean metallicity found by Kirby et al. (2009), $[\text{Fe}/\text{H}]_{\text{mean}} = -1.73$ dex, and that given by Starkenburg et al. (2010), $[\text{Fe}/\text{H}]_{\text{mean}} = -1.77$ dex. Second, for the stars in common, we show in the panels of Fig. 5 the difference between the abundances in Kirby et al. (2009) and our abundances (upper panel), and the difference between the abundances in Starkenburg et al. (2010) and our values (lower panel) plotted against our determinations. In each case there is no indication of any systematic offset in the abundance differences and the standard deviation of the differences are 0.23 dex (upper panel) and 0.15 dex (lower panel), respectively.

Kirby et al. (2009) indicate that a typical error in their metallicity determinations is of order $\varepsilon = 0.10$ dex, while for Starkenburg et al. (2010) the listed typical uncertainty is $\varepsilon = 0.13$ dex. If we assume these typical errors are valid, then we can use them and the dispersions in the abundance differences to provide an alternative estimate of the uncertainty in our abundance determinations. From the comparison with the Starkenburg et al. (2010) values, we derive an estimate of 0.07 dex for our abundance uncertainties, which is quite consistent with that derived above. The comparison with the Kirby et al. (2009) values, however, yields a substantially larger estimate (0.21 dex) for the uncertainty in our abundance determinations that seems at odds with the comparison with the Starkenburg et al. (2010) values and with our internal error estimate. It is possible that Kirby et al. (2009) have underestimated their abundance errors. We therefore adopt a typical abundance error of 0.10 dex for our determinations.

Given the metallicity spread in Scl, there is no straightforward way to decide if a particular Scl star lies on the RGB or on the AGB in the CMD. At fixed luminosity, an AGB star is hotter than an RGB star of the same metallicity leading to weaker lines in the AGB-star spectrum. Consequently, our abundance determination process will underestimate the actual abundance of Scl AGB stars. We can estimate the size of this effect by using our GGC star spectra, noting that the GGCs used are monometallic. Specifically,

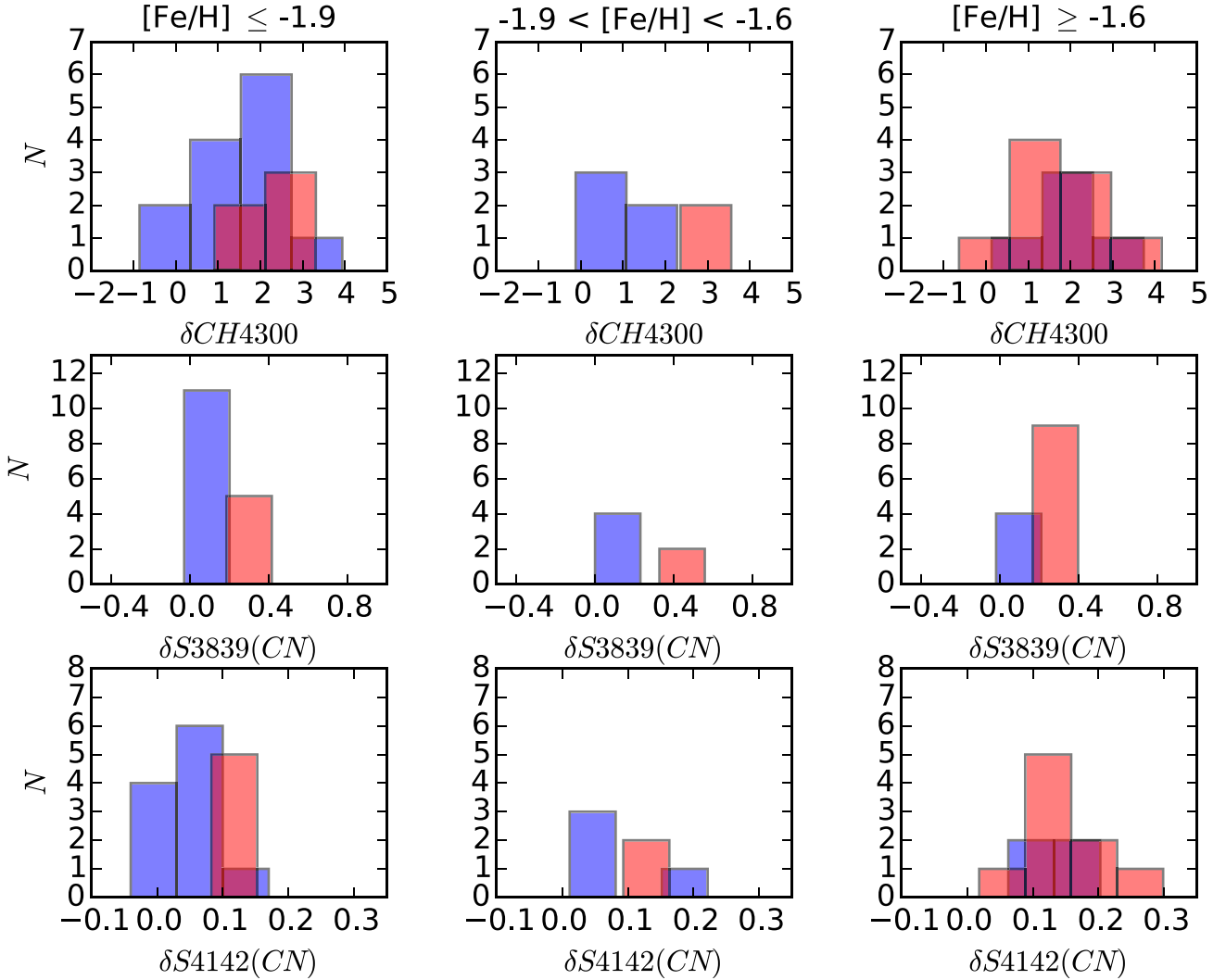


Figure 9. Histograms of $\delta W(G)$ (top row), $\delta S3839$ (middle row), and $\delta S4142$ (bottom row) for the Scl stars. The Scl sample has been separated into three groups of metallicity as shown at the top of the columns. The bin sizes chosen are slightly larger than the index errors in each group of metallicities. CN-weak stars are shown in blue and CN-strong stars in red, and were defined by the middle row of Fig. 8.

in our observed sample for NGC 1851, there are three stars that are readily identified as AGB stars in the cluster CMD, while there are four such stars in the NGC 6752 sample. The mean $[Fe/H]$ for the NGC 1851 AGB stars from our abundance analysis approach is $[Fe/H] = -1.40$ ($\sigma = 0.13$), while for the NGC 6752 AGB stars the mean abundance is $[Fe/H] = -1.75$ ($\sigma = 0.02$). Both these values are about 0.2 dex less than the metallicities given in the Harris (1996) catalogue (see Table 2). In GGCs ~ 20 – 25 per cent of giant branch stars belong to the AGB and we assume that fraction also applies in Scl. Consequently, we must remain aware that our metallicity estimates for ~ 20 – 25 per cent of the Scl sample could be underestimated by up to 0.2 dex.

4 RESULTS

4.1 CH and CN

The GGC abundance anomalies were originally characterized via analysis of red giant spectra covering the CN bands around 3880 Å and 4215 Å, and the CH band at ~ 4300 Å commonly known

as the G band (e.g. Osborn 1971; Norris et al. 1981; Cannon et al. 1998; Carretta et al. 2005). The data revealed that the stars in a given cluster could be classified into two well-separated groups, one CN-strong and the other CN-weak. There is also a well-defined anticorrelation in that the CN-strong stars are relatively CH-weak and vice versa. At the same time spectrum synthesis calculations revealed that the effects are driven by enhanced nitrogen and depleted carbon abundances in the CN-strong population relative to the CN-weak group (e.g. Kraft 1994b; Pancino et al. 2010). To investigate if these GGC effects are also present in the Sculptor red giant data set, we measured the indices $W(G)$, $S(3839)$, and $S(4142)$ as outlined in Section 2.1 for the Scl stars with blue spectra. As noted in Section 3, we then separate the set of index measurements into three metallicity groups using the $[Fe/H]$ values derived from the corresponding red spectra. The IDs, positions, V and $V - I$ photometry, index measures, sodium line strengths (see Section 4.3) and derived metallicities for these stars are listed in Table 7.

For comparison purposes we also measured, in the same way as for the Scl stars, the band strength indices for red giants in three GGCs using the AAOmega blue spectra. The three GGC

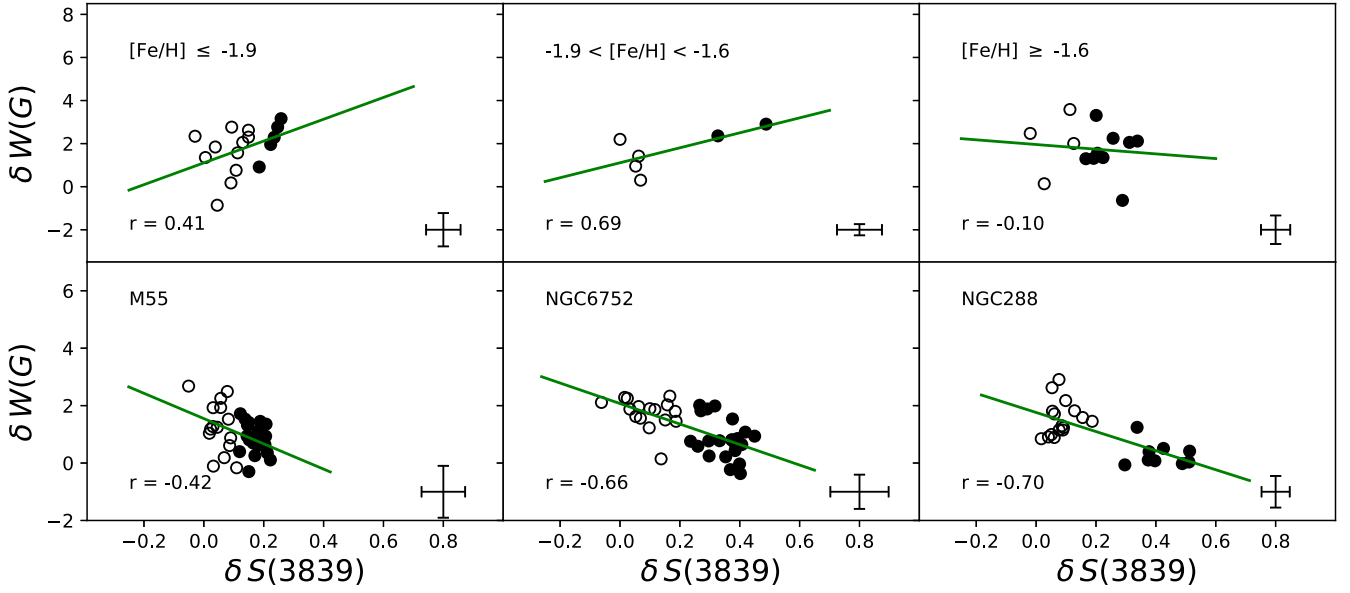


Figure 10. Upper row: the dependence of $\delta S(3839)$ on $\delta W(G)$ for RGB stars of Sculptor with $[Fe/H] \leq -1.9$, $-1.9 < [Fe/H] < -1.6$, and $[Fe/H] \geq -1.6$ dex. Lower: the same quantities for the RGB members of the GGCs M55, NGC 6752, and NGC 288. Filled and empty circles represent CN-strong and CN-weak stars as defined by the middle panels of Figs 8 and 6, respectively. Green lines represent the best fit in each case. Correlation coefficient (r) is shown in each panel. Note the strong anticorrelation between the two parameters for GGC stars. Error bars for each index and data set are shown in the bottom right corner in each panel.

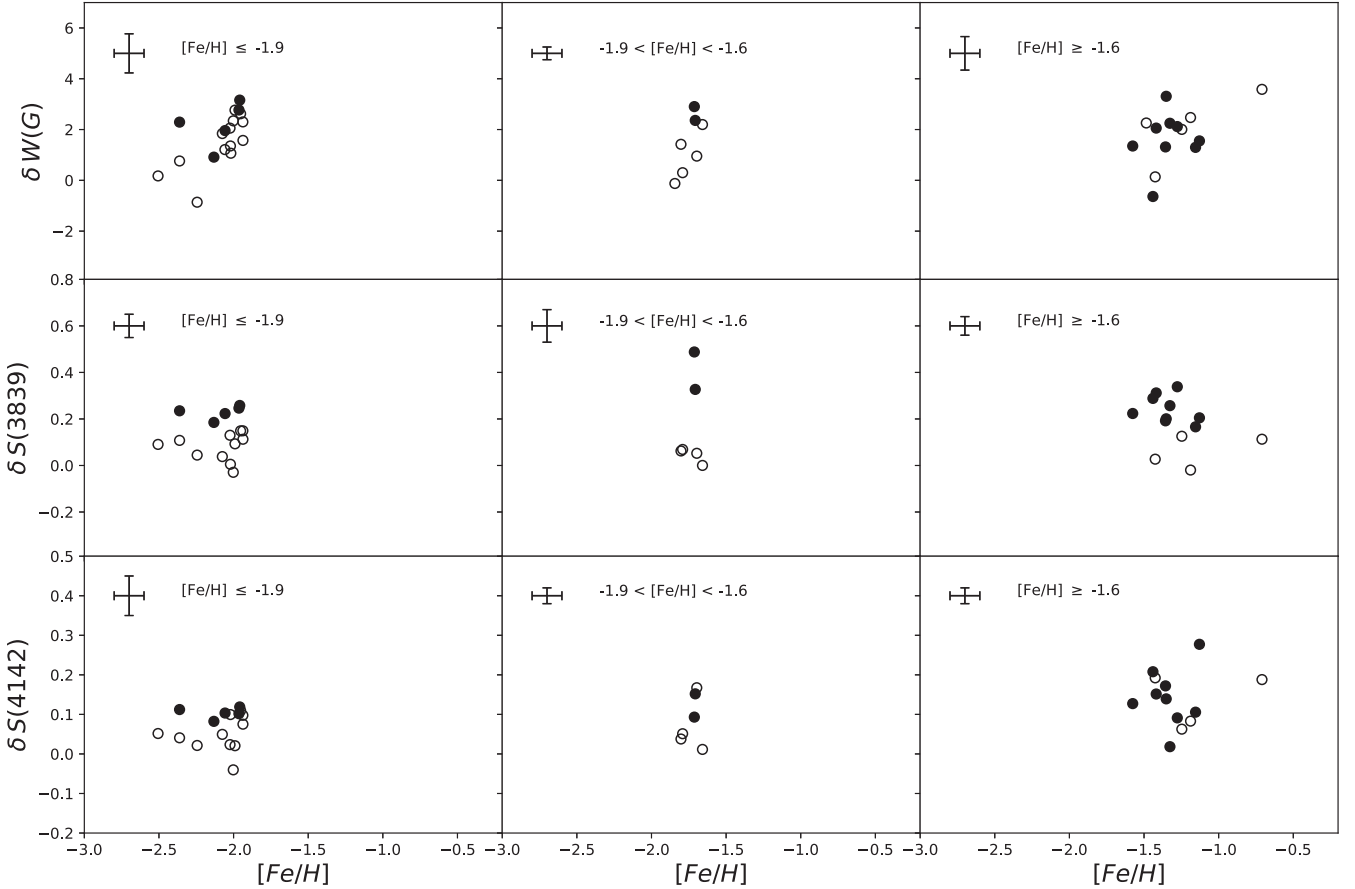


Figure 11. $\delta W(G)$, $\delta S(3839)$, and $\delta S(4142)$ band strength indices versus $[Fe/H]$ for the Scl stars. The range of metallicities for each Scl group is indicated at the top of each panel. Filled and empty circles represent CN-strong and CN-weak stars as defined by the middle panels of Fig. 8. Error bars are shown for the δ values (from Table 3) and for the metallicity values.

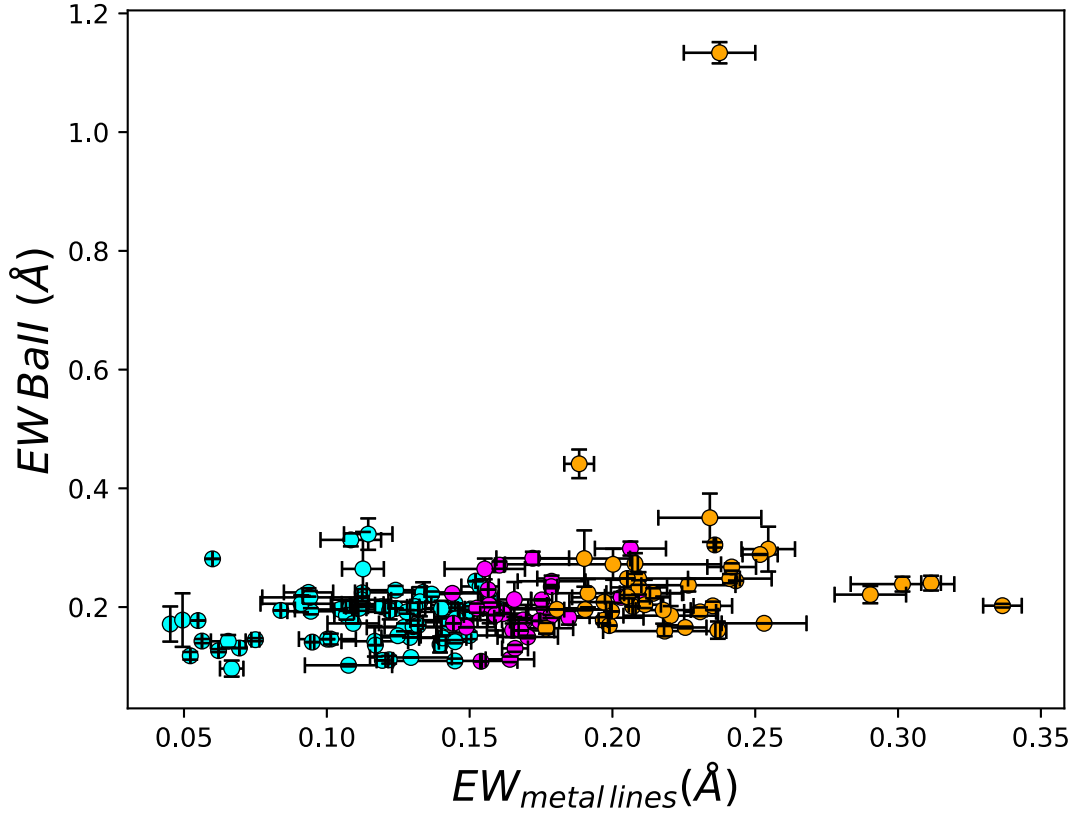


Figure 12. Equivalent width of Barium II line at 6142 Å against equivalent width of metal lines (12 strong lines of calcium, iron, and nickel used in the metallicity determination; see Section 3). For the observed stars, the colour coding refers to different metallicity groups: cyan, magenta, and orange are used for stars with $[\text{Fe}/\text{H}] < -1.9$, $-1.9 \leq [\text{Fe}/\text{H}] \leq -1.6$, and $[\text{Fe}/\text{H}] > -1.6$ respectively. Errors represent the standard deviation of two measurements scaled by $\sqrt{2}$.

Table 4. $[\text{C}/\text{Fe}]$, $[\text{N}/\text{Fe}]$, and $[\text{O}/\text{Fe}]$ abundances used for in synthetic spectra calculations.

	M55	NGC 6752	NGC 288
$[\text{C}/\text{Fe}]_{\text{CN-weak}\star}$	-0.7	-0.6	-0.5
$[\text{N}/\text{Fe}]_{\text{CN-weak}\star}$	-0.5	-0.6	-0.5
$[\text{O}/\text{Fe}]_{\text{CN-weak}\star}$	0.4	0.4	0.4
$[\text{C}/\text{Fe}]_{\text{CN-strong}\star}$	-1.2	-1.1	-1.0
$[\text{N}/\text{Fe}]_{\text{CN-strong}\star}$	0.5	0.4	0.5
$[\text{O}/\text{Fe}]_{\text{CN-strong}\star}$	0.0	0.0	0.0

chosen (M55, NGC 6752, and NGC 288) have metallicities that are comparable to the mean metallicities of the three Scl groups. The resulting GGC band strengths, plotted against $V - V_{\text{HB}}$, are shown in Fig. 6. We use the values of the $S(3839)$ index (middle panels) to classify the GGC stars as CN-strong or CN-weak via a visual inspection of the distributions. As expected, there is a clear separation between the two groups. The figure also shows a green straight line in each panel that represents the lower envelope of the data for each index and cluster. These lines represent an assumed minimum value for the indices at any $V - V_{\text{HB}}$. The slope of these lines was obtained from the best fit for all the stars in each panel and the vertical location was set to encompass the minimum values, given the index errors. Based on these lines, we have defined a parameter δ , similar to the one introduced by Norris et al. (1981), that measures the index displacement at a given V magnitude with respect to the lower envelope. This excess parameter δ minimizes

Table 5. Stellar parameters and derived C, N abundances for a representative subsample of the data.

ID	T_{eff} K	$\log(g)$ dex	ξ_t km s $^{-1}$	$[\text{Fe}/\text{H}]$ dex	$[\text{C}/\text{Fe}]$ dex	$[\text{N}/\text{Fe}]$ dex	$[\text{O}/\text{Fe}]$ dex
Scl-0272	4558	1.48	1.74	-2.50	-0.75	0.65	0.4
Scl59	4674	1.24	1.82	-2.13	-0.55	0.43	0.0
Scl81	4635	1.30	1.79	-2.07	-0.65	0.87	0.4
Scl38	4422	1.65	1.68	-2.05	-0.95	0.33	0.0
Scl-1490	4582	1.41	1.76	-2.02	-0.84	-0.30	0.4
11.1-6268	4493	1.52	1.72	-1.80	-0.73	0.08	0.4
Scl-1020	4518	1.43	1.75	-1.71	-0.40	0.25	0.0
Scl-0492	4372	1.42	1.76	-1.79	-0.87	-0.6	0.4
Scl-0247	4483	1.50	1.73	-1.70	-0.83	0.0	0.0
Scl-0268	4518	1.50	1.73	-1.69	-0.93	0.07	0.4
Scl23	4814	1.26	1.81	-1.65	-0.33	0.00	0.4
10.8-4149	4327	1.65	1.68	-1.35	-0.8	-0.51	0.0
Scl20	4406	1.50	1.73	-1.27	-0.95	-0.30	0.0
Scl-0437	4476	1.40	1.76	-1.24	-0.72	-0.46	0.4
Scl-0276	4687	1.38	1.77	-1.18	-0.61	-0.34	0.4
Scl-0233	4396	1.58	1.71	-1.15	-0.92	-0.30	0.0

the effects on the band strength indices of the changing temperatures and surface gravities of the stars.

Nevertheless, each Scl metallicity group does contain a range in abundance and, at fixed $V - V_{\text{HB}}$, the higher metallicity stars in each group will have lower T_{eff} , and vice versa, and this can potentially affect the range of line strength indices present. We have explored

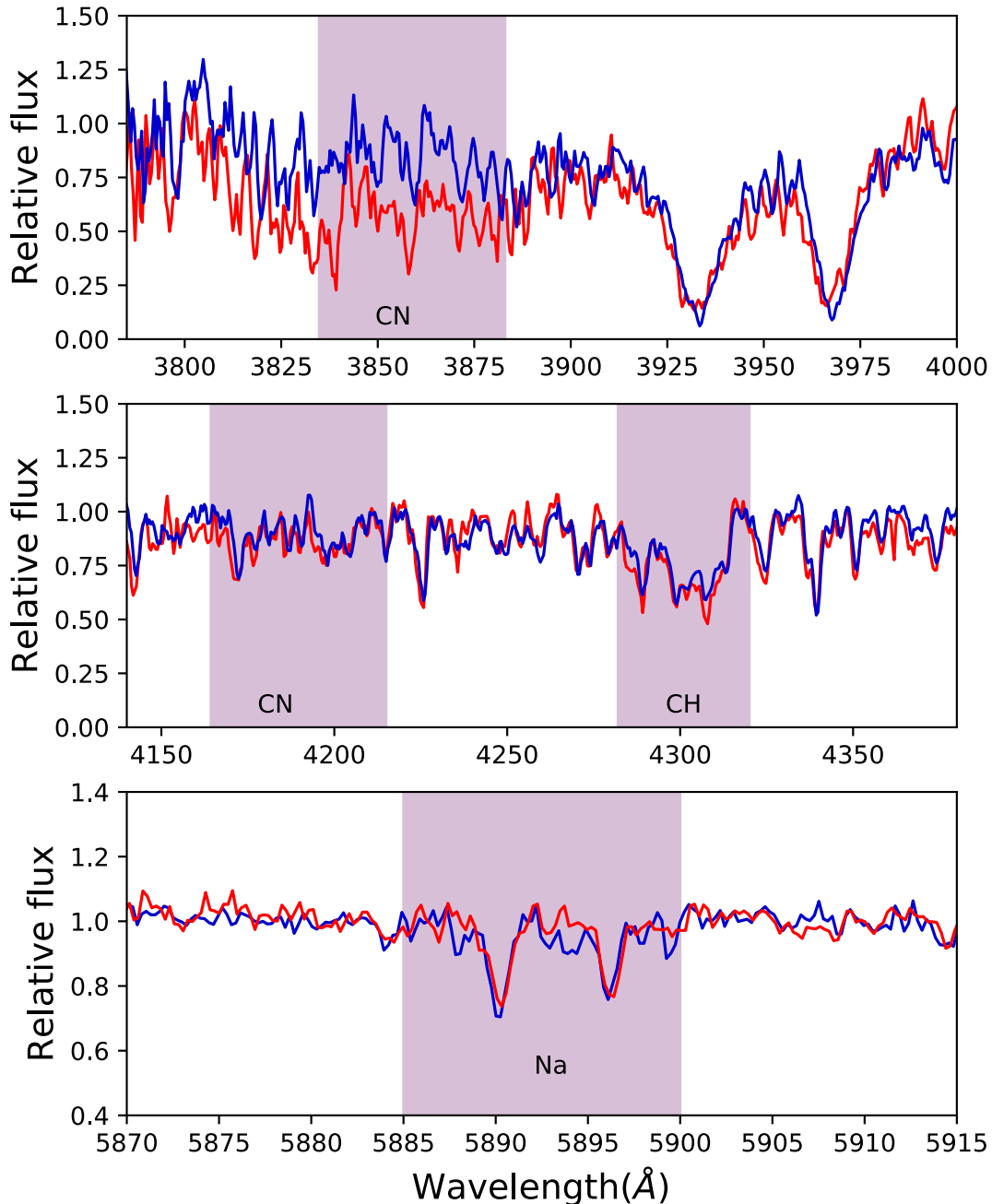


Figure 13. Normalized spectra of Scl-0492 and Scl-0247, the stars highlighted in magenta in the central panel of Fig. 8. The location of the CH, at $\lambda \approx 4300$ Å, and the CN, at $\lambda \approx 3883$ Å and $\lambda \approx 4215$ Å, bands and Na, at $\lambda \approx 5889$ Å and $\lambda \approx 5895$ Å, are shown by the shaded regions. The blue spectrum is Scl-0492 (CN-weak), while the red spectrum is Scl-0247 (CN-strong).

the consequences of this effect by measuring the indices on a number of synthetic spectra that have the same resolution as the observed data. Specifically, we note for each Scl metallicity group that the variation in $V - I$ at fixed $V - V_{\text{HB}}$ is typically ± 0.2 , ± 0.17 , and ± 0.19 mag for the metal-poor, intermediate-metallicity, and metal-rich groups, respectively (see Fig. 1), presumably driven primarily by the metallicity ranges. These colour variations were obtained via low-order polynomial fits to the giant branch photometry. Then using the $T_{\text{eff}}:V-I:[\text{Fe}/\text{H}]$ calibrations from Ramírez & Meléndez (2005), the mean metallicity for each group, and a typical $V - I$ value, the colour variations correspond to the temperature variations of $\sim \Delta 240$ K, $\sim \Delta 210$ K, and $\sim \Delta 240$ K, respectively. We then

calculated for each metallicity group the $W(G)$, $S(3839)$ and $S(4142)$ indices from synthetic spectra assuming the mean metallicity of each group with upper and lower temperature values that differ from the adopted values by these offsets, assuming the mean metallicity of each group. For the most metal-poor group, the resulting changes were ~ 0.85 Å for $W(G)$, ~ 0.024 mag for $S(3839)$, and ~ 0.017 mag for $S(4142)$, respectively (higher values for lower temperatures). For the intermediate-metallicity and metal-rich groups, the changes were ~ 0.69 Å, ~ 0.029 mag and ~ 0.017 mag, and ~ 0.60 Å, ~ 0.027 mag, and ~ 0.017 mag, respectively. Comparison with the panels of Fig. 8 shows that these changes are substantially smaller than the observed index ranges for each metallicity group, indicating that

the range in metallicity (and thus in T_{eff} at fixed $V - V_{\text{HB}}$) within each grouping is not a major contributor to the observed range in index values.

Fig. 7 then shows histograms of the δ parameter for each index in the GGC sample. The histogram of the $\delta S(3839)$ parameter demonstrates the well-established bimodality of the CN-band strength for these GGCs. The other panels in Figs 6 and 7 show that the bimodality of the CN-band strength is also seen in the $S(4142)$ index, particularly for the two more metal-rich GGCs, and that there is a general anticorrelation between the CN- and CH-band strengths. The errors in the indices have been estimated via the reasonable assumption that in the absence of observational errors, the CN-weak sequences in each cluster should show zero index scatter; hence the rms about a line fitted to the CN-weak sequences provides a measure of the index errors. The sizes of the error estimates are indicated on the panels of Fig. 6.

Figs 6 and 8 show the band strength indices for the Sculptor stars plotted against $V - V_{\text{HB}}$ magnitude, again using $V_{\text{HB}} = 20.35$ for Scl (Tolstoy et al. 2001). Shown also, as green dashed lines, are the adopted lower envelope lines for the Scl data where we have used the same slope as the corresponding lower envelope lines in the panels of Fig. 6. These are also plotted in the figure as green solid lines; in most of the cases there is a small offset between the line positions. As for the GGC data, we have measured the δ values for each index and metallicity group, and the histograms are shown in Fig. 9. We have then classified the Scl stars, by eye, as ‘CN-strong’ or ‘CN-weak’ on the basis of the $\delta S(3839)$ values. The bimodality is not as clear-cut as it is for the GGC stars, at least in part because the index errors are larger for the Scl stars, which may lead to a blurring of any bimodality present. In effect, it is the stars with the larger values of $\delta S(3839)$ that we have classified as CN-strong. Only in the case of the intermediate metallicity group is there an indication of a gap in the $\delta S(3839)$ distribution that might indicate a bimodal distribution. The errors in the index values for the Scl stars were estimated by making use of the fact that for each Scl star there are generally two measures of each index from the two GMOS-S spectra taken at slightly different central wavelengths. The standard deviation of the differences (scaled by $\sqrt{2}$) within each metallicity group was then employed as the index measurement uncertainty; these values are shown in the panels of Fig. 8. We note for completeness that we have not included in this analysis the star Scl-1013644, which has very strong CN and CH bands. This star was identified as a CEMP-star and has been discussed in Salgado et al. (2016).

In the panels of Fig. 8, the lowest metallicity group shows good consistency between the $S(3839)$ and $S(4142)$ indices – the stars classified as CN-strong stars in the $S(3839)$ panel also have larger values of $S(4142)$. We have checked that this is not a metallicity effect – the average metallicity for the CN-strong stars in this group is similar to that for CN-weak stars. However, the $W(G)$ index in this lowest metallicity group does not show any convincing indication that the CN-strong stars are significantly weaker in $W(G)$, as in seen in the comparison GGC M55. Nevertheless, based on the mean $W(G)$ index error for this group, it does appear that there is a significant real dispersion in the $W(G)$ values.

The same results are seen in the intermediate metallicity group – the $S(4142)$ indices are broadly consistent with the classification based on the $S(3839)$ indices, but there is no indication that the Scl CN-strong stars are CH-weak in contrast to what is evident in the data for the corresponding GGC NGC 6752. We illustrate this in the panels of Fig. 13, where we show the continuum-normalized velocity-corrected observed spectra for the stars Scl-0247 (CN-strong) and Scl-0492 (CN-weak). These stars are represented by

the filled and open magenta circles in Fig. 8. The stars have similar colours and $V - V_{\text{HB}}$ magnitudes and thus similar T_{eff} and $\log g$ values. Our derived metallicities are also similar: we find $[\text{Fe}/\text{H}] = -1.70$ for Scl-0247 and $[\text{Fe}/\text{H}] = -1.79$ for Scl-0492. The spectra shown in Fig. 13 confirm the inferences from the indices in Fig. 8: Scl-0247 has notably stronger 3880 Å CN-strength but the differences at the 4215 Å CN-band and, in particular, at the G-band (CH, ~ 4300 Å) are much less substantial. We defer to Section 4.2 a discussion of the C and N abundances that can be derived from these spectra via synthetic spectrum calculations. Fig. 13 also shows, in the bottom panel, a comparison of the two spectra in the vicinity of the Na D lines. The Na D lines are clearly also very similar in strength, an outcome that will be discussed further in Section 4.3.

As for highest abundance group of Scl stars, the results are not as clear-cut. The majority stars in this group are classified as CN-strong using the $S(3839)$ indices, but the CN-weak stars are not generally CN-weak in the $S(4142)$ panel. Further, there is a broad range in the $W(G)$ values with no obvious separation of the CN-weak/CN-strong stars.

In Fig. 10 we show plots of $\delta W(G)$ against $\delta S(3839)$ for the three metallicity groups of Scl stars and for the three comparison GGCs. The δ values have been measured using the appropriate lower envelope lines, and their errors are given in Table 3. The error in each delta was calculated as a combination of the error in the index plus the uncertainty in the location of the lower envelope line. The bottom row in the figure confirms the well-established result that in GGCs, CN- and CH-band strengths are anticorrelated. The upper rows of the figure indicate, however, that this is evidently not the case for the Scl stars – indeed the opposite appears to be the case in that either indices are not correlated (upper right panel), or there is a trend for the CN-strong stars to have relatively stronger CH bands (left and middle panels).³ This can be corroborated by the values of the correlation coefficient r , which has values of 0.41, 0.69, and -0.10 for metal-poor, intermediate-metallicity, and metal-rich groups, respectively. The correlation coefficient assumes values in the range from -1 to $+1$, where -1 indicates a strong negative relationship between the data and $+1$ indicates a strong positive relationship.

We have sought confirmation of these results by making use of the $\text{CH}(\lambda 4300)$ and $S(3839)$ indices from Lardo et al. (2016). We binned their Scl stars into the same metallicity groups as used here and employed their index values to generate panels equivalent to those in the upper part of Fig. 10. We find that the resulting $\delta \text{CH}(4300)$ versus $\delta S(3839)$ plots bear considerable resemblance to those for our data. In particular, as in Fig. 10, there is only a weak positive correlation between these two quantities: the correlation coefficients are $r = 0.38$, 0.56 , and 0.10 for the metal-poor, intermediate-metallicity, and metal-rich groups, respectively, values that are very similar to those found for our data.

³At fixed metallicity and T_{eff} , the $W(G)$ and $S(3839)$ indices, and their corresponding δ values, might naturally be expected to increase with increasing carbon abundance. We have investigated this effect by measuring the indices on a series of synthetic spectra with varying carbon abundances. Specifically, we adopted the parameters $T_{\text{eff}} = 4500$ K, $\log g = 1.0$, and $[\text{Fe}/\text{H}] = -1.5$ dex, and calculated the indices from synthetic spectra with carbon abundance ratios $[\text{C}/\text{Fe}]$ of -1.0 , -0.5 , 0.0 , 0.5 , and 1.0 dex. We find that increasing the carbon abundance does increase both indices, but with a slope $\Delta W(G)/\Delta S(3839)$ that is substantially steeper than those exhibited by the positive correlations in the upper panels of Fig. 10. We conclude that the relations in the upper panels of Fig. 10 are not driven solely by changing carbon abundances.

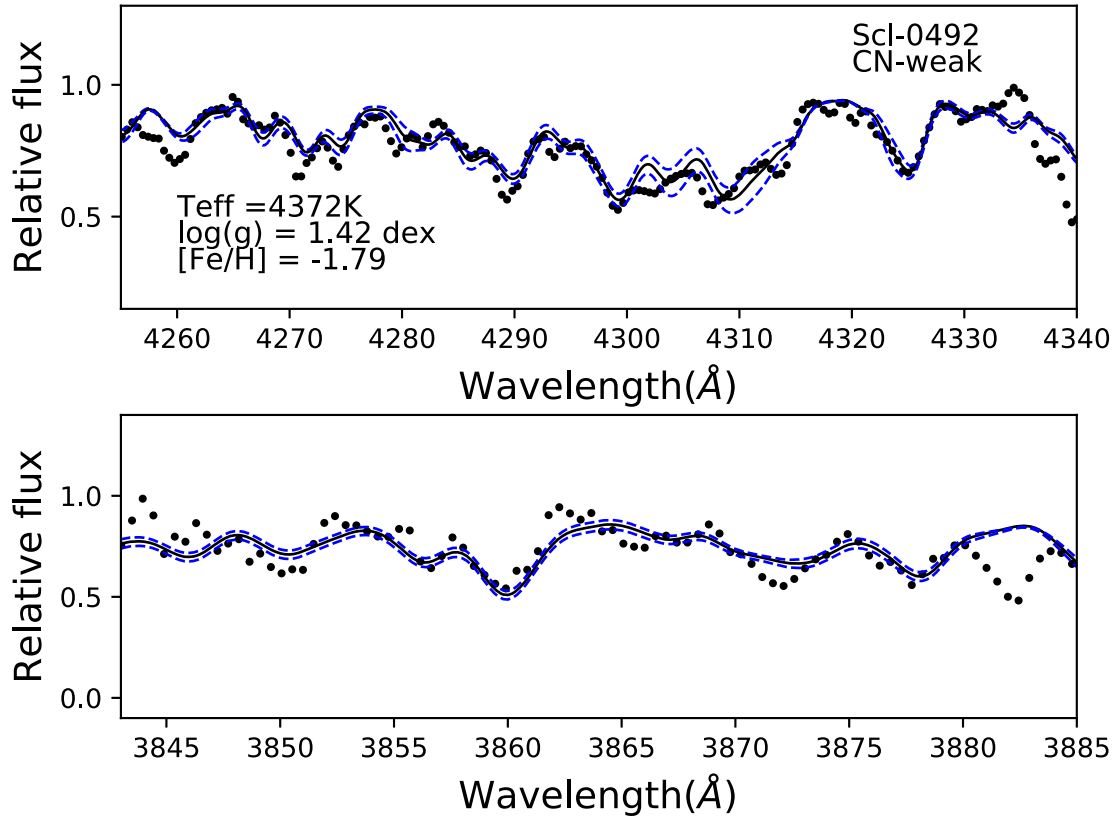


Figure 14. Spectrum synthesis of CH (top panel) and CN (bottom panel) features for Scl-0492 (CN-weak). In both panels the observed spectrum is represented by solid dots. Upper panel: the solid line represents the best abundance fit that has $[C/Fe] = -0.87$ assuming $[O/Fe] = +0.4$. The dashed blue lines show $[C/Fe]$ values ± 0.16 dex about the central value. Lower panel: the solid line represents the best abundance fit that has $[N/Fe] = -0.6$ and $[C/Fe] = -0.87$, assuming $[O/Fe] = +0.4$. The dashed blue lines show nitrogen values ± 0.3 dex from the best fit.

In order to understand if the apparent positive correlation between CN and CH for the Scl stars could be an effect of the metallicity range in each Scl group, we have plotted the δ values for the indices against our estimation of the metallicities of the individual stars. We decided to use δ values in order to minimize the effects of the different temperatures and surface gravities of the Scl stars. In Fig. 11 no obvious trends are visible, on the contrary there are substantial ranges in all the δ values, which are similar across all three metallicity groups. If we instead use $[Fe/H]$ values for the stars from other sources, e.g. Kirby et al. (2009) and Starkeburg et al. (2010), the outcome is essentially unaltered; we conclude that overall metallicity is not responsible for the spreads in the CN and CH indices.

In the next sub-sections we discuss each index in further detail and compute synthetic spectra to investigate the abundance differences implied by the range in index values.

4.1.1 $S(3839)$ index

The $S(3839)$ index for the lowest metallicity group of Scl stars shows a range that is similar to the range shown by the M55 red giants (see Fig. 6); in both cases the range is about ~ 0.2 mag. The average of the observational errors in this group of Scl stars is $\epsilon \approx \pm 0.05$ mag, which is similar in size to the GGC data for M55. Therefore, a genuine dispersion in the index values of these Scl stars may be present.

For the intermediate metallicity group we have a relatively small sample of Scl stars. However, the index values appear to have a

real spread whose range is comparable to that seen for the GGC NGC 6752 – in both cases the range in $S(3839)$ is ~ 0.3 mag. The cluster NGC 6752 shows a very clear bimodality (see Fig. 6) but the limited sample size for Scl makes it difficult to establish the presence or absence of a similar bimodality. We note also that the overlap in luminosity between the NGC 6752 and the Scl samples is limited: the Scl stars are all more luminous than $V - V_{HB} = -2.5$ while the number of NGC 6752 stars in this range is small and no CN-strong stars were observed. As regards the most metal-rich group of Scl stars, they appear to have a smaller range in this index than is shown by the red giants in the comparison GGC NGC 288: the range for the Scl stars is about ~ 0.3 mag while that for the cluster is ~ 0.45 mag. Further, the distribution of the Scl star index values is evidently not obviously bimodal, whereas the cluster data clearly are. This difference does not seem to be a consequence of the slightly larger errors for the Scl stars ($\epsilon \approx \pm 0.05$ dex) as compared to the NGC 288 stars ($\epsilon \approx \pm 0.04$ dex). Further, as for NGC 6752 and the intermediate metallicity Scl stars, there are essentially no NGC 288 stars in the same range of $V - V_{HB}$ as for the metal-rich Scl stars. Indeed ~ 46 per cent of the stars in the Scl metal-rich group are more metal-rich and cooler than the NGC 288 stars.

4.1.2 $S(4142)$ index

The $S(4142)$ index for M55 in GGCs panels of Fig. 6 does not yield any additional information about the behaviour of CN in the cluster stars, but this is not unexpected given the relatively low metallicity of the cluster. This is also the case for the Scl stars in

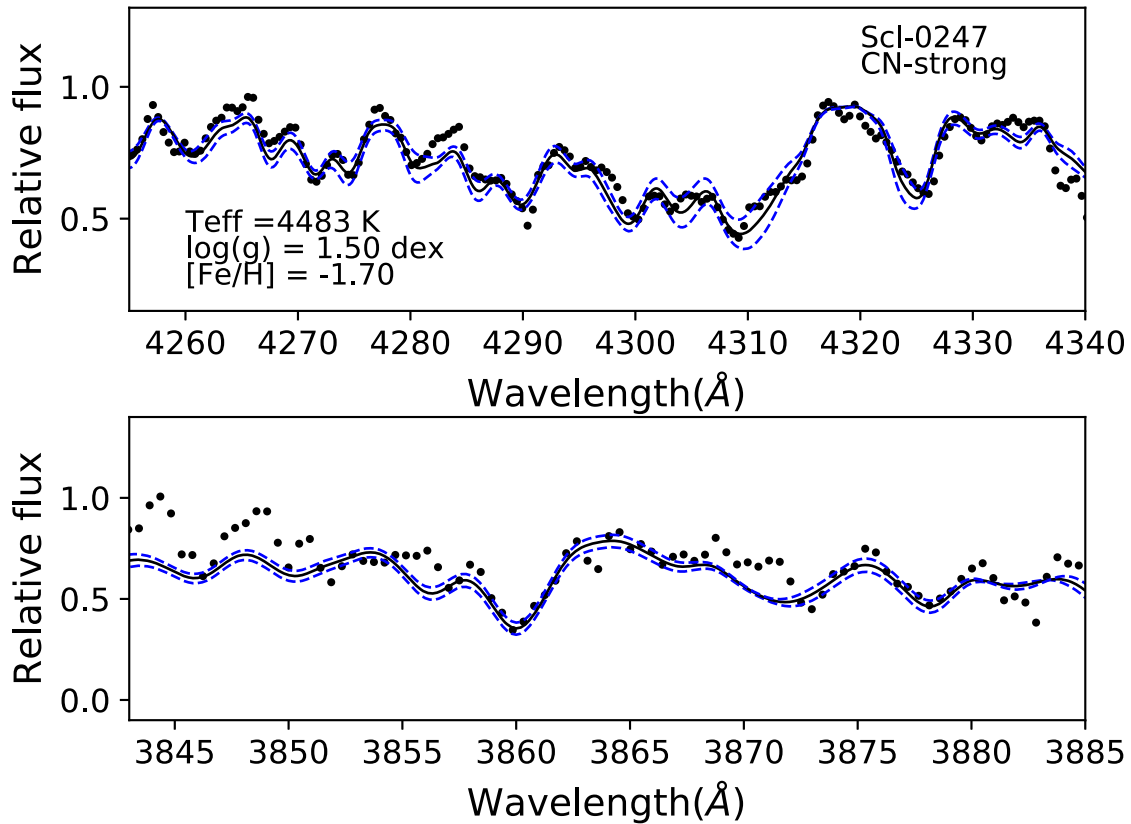


Figure 15. Spectrum synthesis of CH (top panel) and CN (bottom panel) features for Scl-0247 (CN-strong). In both panels the observed spectrum is represented by solid dots. Upper panel: the solid line represents the best abundance fit that has $[C/Fe] = -0.83$ assuming $[O/Fe] = 0.0$. The dashed blue lines show carbon values ± 0.17 dex about the central value. Lower panel: the solid line represents the best abundance fit with $[N/Fe] = +0.00$ and $[C/Fe] = -0.83$, assuming $[O/Fe] = 0.0$. The dashed blue lines show nitrogen values ± 0.3 dex from the best fit.

the low metallicity group although there is a tendency for the stars classified as CN-strong from the $S(3839)$ index to also have higher $S(4142)$ indices. Based on the range of ~ 0.15 mag and the average index error $\varepsilon \approx \pm 0.01$ mag, we conclude that there is a real spread in the index values for this group of Scl stars. We note, however, that the $S(4142)$ errors for the Scl stars are notably smaller than those computed for the GGC stars despite the generally lower S/N of the Scl spectra. This suggests that the derived $S(4142)$ index errors for these Scl stars may be underestimated.

At intermediate metallicity, the data for the GGC NGC 6752 shows a clear separation of the CN-strong and CN-weak groups, demonstrating that at this $[Fe/H]$ there is sufficient sensitivity to detect variations in CN-band strength through the $S(4142)$ index. We note that the two Scl stars that were classified as CN-strong by the $S(3839)$ index values also appear relatively CN-strong in this panel. We caution against overinterpretation of this panel; however, as there is also an Scl star with strong $S(4142)$ that is CN-weak in the $S(3839)$ panel. At the highest metallicities, in the GGC NGC 288 the CN-weak/CN-strong stars defined by the $S(3839)$ index are generally in their expected locations in the $S(4142)$ panel of Fig. 6, but the separation is not as clear-cut. This is also the case for the metal-rich Scl group – the CN-strong and CN-weak stars classified by the $S(3839)$ index are intermingled in the $S(4142)$ panel.

4.1.3 The G band

The first row of Fig. 6 shows in a quite convincing way the expected result for GGCs: that stars considered as CN-strong lie low in

the $(W(G), V - V_{HB})$ plane, consistent with lower $[C/Fe]$ values (see Section 4.1.4). As regards the Scl stars, in general there is little evidence for a CN/CH anticorrelation in the upper panels of Fig 8, and thus there is a clear difference with respect to the GGCs. Nevertheless, given the error estimates for the $W(G)$ values, it does appear that there is a real spread in the $W(G)$ values in all three Scl metallicity groups. Specifically, the observed standard deviations of the $W(G)$ values are $\sigma = 0.96, 0.98,$ and 1.02 \AA , for the metal-poor, intermediate, and metal-rich groups, respectively. Subtracting in quadrature the mean error in $W(G)$ ($\varepsilon = 0.12, 0.21,$ and 0.17 \AA), the implied intrinsic dispersions in $W(G)$ are then $\sigma_{\text{int}} = 0.95, 0.95,$ and 1.00 \AA for the three Scl metallicity groups. The intrinsic dispersion in the $W(G)$ values are presumably driven by intrinsic variations in $[C/Fe]$ on the Scl red giant branch as discussed by Lardo et al. (2016).

Some stars in this figure seem to be both CN-strong and CH-strong, which might be an indicator of a possible CEMP classification: certainly the CEMP-s Scl star (Scl-1013644) discussed in Salgado et al. (2016) is both CN- and CH-strong. To investigate whether there are any other candidate CEMP-s stars in our Scl sample, we measured the strength of the $\lambda 6142 \text{ \AA}$ Ba II line, $W(\text{Ba II})$, in the red spectra for the full sample of Scl giants. The results are shown in Fig. 12, where it is evident that aside from the star Scl-1003644, which has a very strong Ba II line (Salgado et al. 2016), no other Scl giants in our sample possess anomalously strong Ba II lines that would suggest a CEMP-s classification. Fig. 12 also shows that there is a correlation between the $W(\text{Ba II})$ values and equivalent width of the combined metal

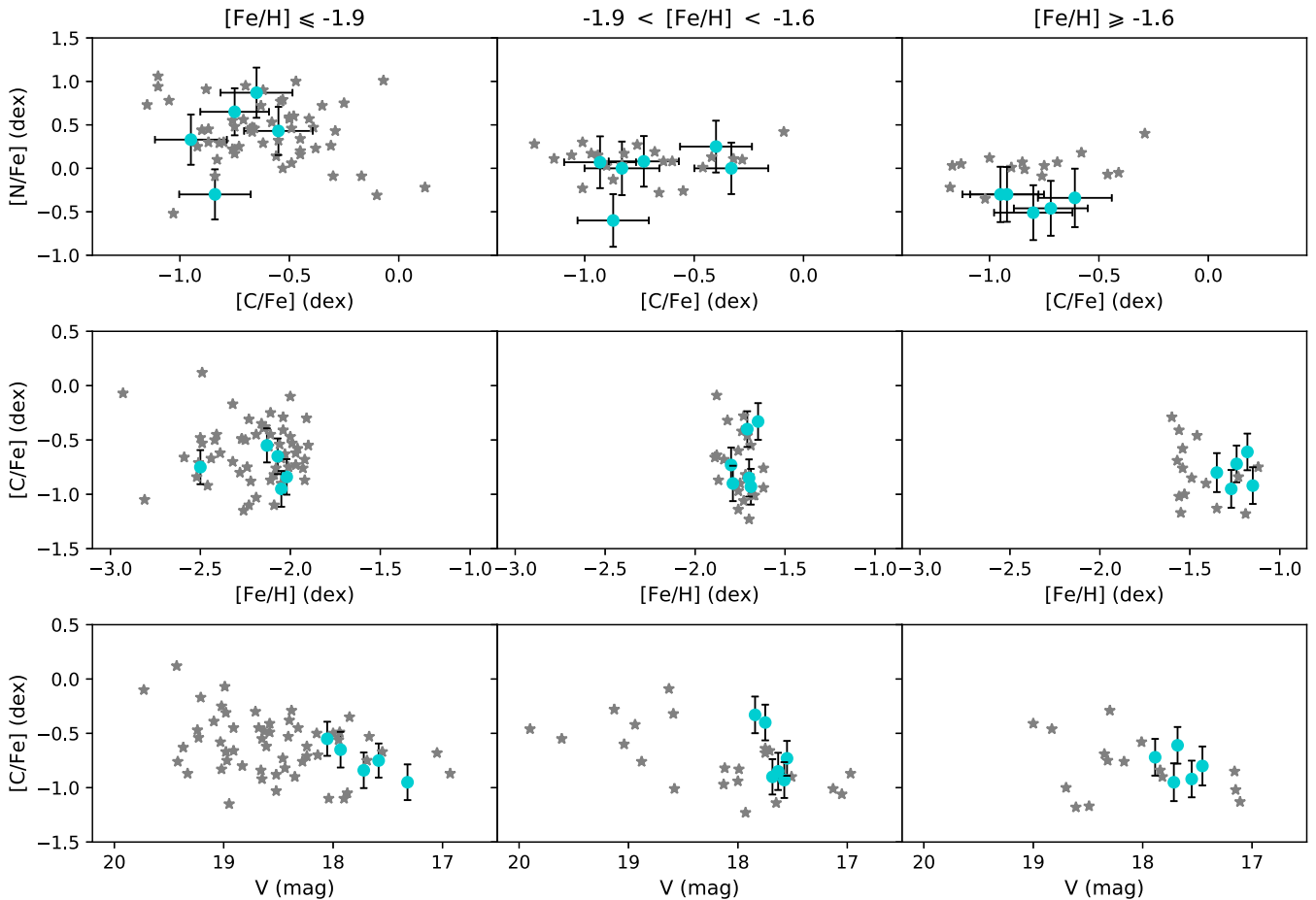


Figure 16. Comparison between the Sculptor stars from Lardo et al. (2016) (grey-stars) and a representative subset of our sample (cyan-filled circles with error bars). The stars have been separated into three groups of metallicities: $[\text{Fe}/\text{H}] \leq -1.9$, $-1.9 < [\text{Fe}/\text{H}] < -1.6$, and $[\text{Fe}/\text{H}] \geq -1.6$ dex. Upper row: the relation between $[\text{C}/\text{Fe}]$ and $[\text{N}/\text{Fe}]$ abundances. Middle row: $[\text{C}/\text{Fe}]$ abundances as function of metallicities $[\text{Fe}/\text{H}]$. Lower row: $[\text{C}/\text{Fe}]$ against V magnitude.

lines used to determine the metallicities of the Scl stars, as expected since in general we expect the barium abundance to scale with metallicity.

4.1.4 Spectrum synthesis

A number of studies have shown that the observed CN/CH band-strength anticorrelation in GGC red giants is driven by anticorrelated changes in the $[\text{N}/\text{Fe}]$ and $[\text{C}/\text{Fe}]$ abundances. Generally, relative to the CN-weak stars, the CN-strong stars have increased $[\text{N}/\text{Fe}]$ by factors of 4–10 \times and depletions in $[\text{C}/\text{Fe}]$ of 2–3 \times for a given assumption regarding $[\text{O}/\text{Fe}]$ (e.g. Smith, Briley & Harbeck 2005; Schiavon et al. 2016b). To investigate the abundance ranges implied by our data, we have computed a number of synthetic spectra for pairs of $[\text{N}/\text{Fe}]$, $[\text{C}/\text{Fe}]$, and $[\text{O}/\text{Fe}]$ and for T_{eff} , $\log g$, and $[\text{Fe}/\text{H}]$ values that follow the RGBs of the three comparison GGCs. The analysis was performed using the local thermodynamic equilibrium (LTE) spectrum synthesis program MOOG (Snedden 1973; Sobeck et al. 2011) and ATLAS9 model atmospheres (Castelli & Kurucz 2003). The solar values used were $T_{\text{eff}, \odot} = 5790$ K, $\log g_{\odot} = 4.44$, and $M_{\text{bol}, \odot} = 4.72$. The effective temperatures T_{eff} were obtained using the reddening corrected RGB colours and the T_{eff} -colour calibration of Alonso, Arribas & Martínez-Roger (1999). The bolometric magnitudes were derived from the RGB V magnitudes and

the reddenings and distance moduli listed in the most recent version of the Harris (1996) catalogue for the GGCs (see Table 2). For Scl, a reddening of $E(B - V) = 0.018$ and a distance modulus of 19.67 (Pietrzyński et al. 2008) were used. We assumed $M_* = 0.8$ solar masses for the RGB stars and then calculated the surface gravities from the stellar parameters. Finally, the synthetic spectra were smoothed to the resolution appropriate for each set of observations.

Once the set of synthetic spectra was available, we measured the $W(G)$, $S(3839)$, and $S(4142)$ indices. The resulting band-strength index values were then used to define the shaded regions in the panels of Fig. 6: in the $S(3839)$ and $S(4142)$ panels the upper boundary is for the assumed abundances for the CN-strong stars, and the lower boundary is for the CN-weak abundances (see Table 4). The reverse is the case for the $W(G)$ panel. Generally the agreement between the synthetic spectra predictions and the location of the observed cluster populations is satisfactory, confirming the expected abundance differences between the populations. We note that it was necessary to adopt $[\text{C}/\text{Fe}] \approx -0.6$ for the CN-weak stars (see Table 4) as the predicted $W(G)$ values were substantially too large with $[\text{C}/\text{Fe}] = 0.0$ dex. This low value of $[\text{C}/\text{Fe}]$ is not inconsistent with the predictions of evolutionary mixing on the RGB as discussed, for example, by Placco et al. (2014).

We note also that our values for the nitrogen abundances for the CN-weak GGC red giants are comparable with other determinations in the literature. For example, Yong et al. (2008) found for NGC

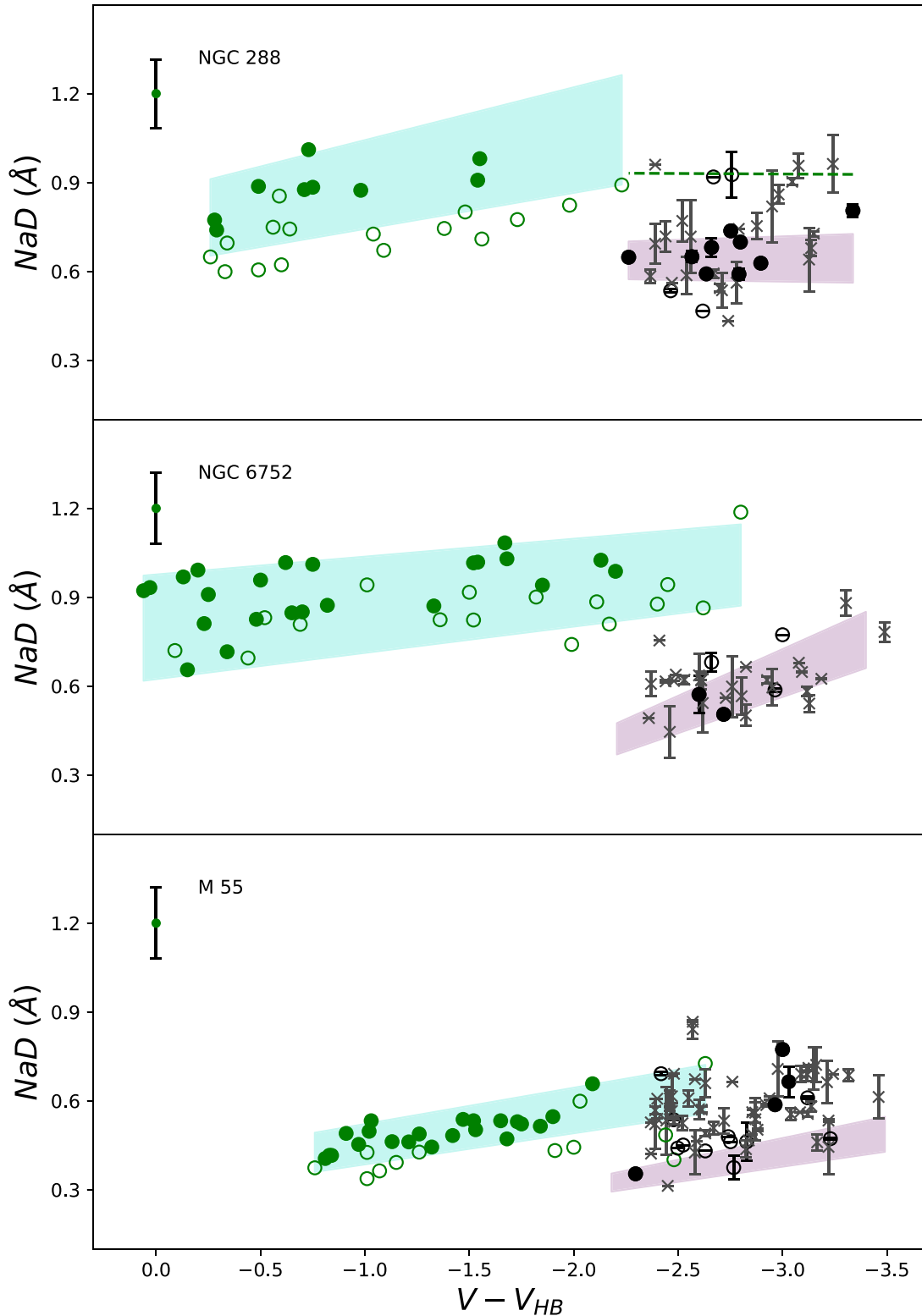


Figure 17. The relation between CN band and Na D line strengths for RGB stars in the comparison GGCs and in Scl. The three panels are for the three GGCs and for Scl stars in the corresponding metallicity groups, with the highest metallicity in the top panel and the lowest in the bottom panel. The GGC stars are shown as green circles, filled for CN-strong stars and open for CN-weak stars. A typical error bar for the GGC $W(\text{NaD})$ measurements is shown in the upper left of each panel. The green-shaded region represents the range in $W(\text{NaD})$ for a range in $[\text{Na}/\text{Fe}]$ of 0.5 dex derived from spectrum synthesis calculations. The Sculptor stars with blue spectra are shown as black circles, filled for CN-strong and open for CN-weak. Grey x-symbols are used for the Scl stars that lack blue spectra. Individual uncertainties are shown for each star. The pink-shaded region also shows the extent of a 0.5 range in $[\text{Na}/\text{Fe}]$, but with a lower $[\text{Na}/\text{Fe}]$ for the upper and lower limits than for the GGCs. See the text for details. The green-dashed line in the upper panel represents $[\text{Na}/\text{Fe}] = 0.0$ at $[\text{Fe}/\text{H}] = -1.25$ dex.

Table 6. Details of synthesis [Na/Fe].

	Lower limit [Na/Fe]	Upper limit [Na/Fe]	[Fe/H] ^a
NGC 288	-0.1	0.4	-1.32
NGC 6752	0.1	0.6	-1.54
M 55	-0.5	0.0	-1.94
Scl [Fe/H] ≥ -1.6	-1.0	-0.5	-1.25 and -1.55
Scl -1.9 < [Fe/H] < -1.6	-1.0	-0.5	-1.63 and -1.68
Scl [Fe/H] ≤ -1.9	-1.0	-0.5	-1.90 and -1.95

Note. ^aMetallicities assumed in generating the synthesis spectra.

6752 values of nitrogen from [N/Fe] = -0.43 upwards, while for NGC 7078 (M15), which has [Fe/H] = -2.37, Trefzger et al. (1983) found [N/Fe] ≈ -0.6 dex. Similarly, Suntzeff (1981) found [N/Fe] = -0.4 for CN-weak stars in NGC 5272 (M3) and NGC 6205 (M13) both of which have [Fe/H] ≈ -1.5 dex. The specific [C/Fe], [N/Fe], and [O/Fe] abundances adopted for the CN-weak and CN-strong populations in each GGC are listed in Table 4, noting that the [O/Fe] values used are assumptions consistent with observations of O-strong (Na-weak) and O-weak (Na-strong) stars in GGCs as we have no means to directly determine oxygen abundances from our data.

To investigate the extent to which the Scl stars show similar [C/Fe] and [N/Fe] variations to the GGC stars, we smoothed the synthetic spectra to the lower resolution of the Scl blue spectra and recomputed the values the band-strength indices. The outcome is shown as the shaded regions in the panels of Fig. 8. For the *S*(3839) index, the majority of the Scl stars, in all the metallicity groups, lie below the lower boundary of the shaded region, with only the CN-strong objects reaching into the shaded region. Nevertheless the range in the Scl index values is approximately comparable to the width of the shaded region. Similarly, in the *W*(*G*) panels, again the Scl stars lie below the shaded region in all three metallicity groups, although, like the situation for *S*(3839), the observed range of the Scl data points is comparable to, or perhaps somewhat larger than, the width of the shaded region. Taken at face value, this would seem to indicate that the [C/Fe] values for these luminous Scl stars, which lie near the RGB-tip, are yet lower than the [C/Fe] ≈ -1.0 dex assumed for the GGC CN-strong stars. Whether this additional carbon depletion is sufficient to reduce the values of the synthetic *S*(3839) indices into the observed region is unclear as CN-band strength is sensitive to both [C/Fe] and [N/Fe]. The panels for the *S*(4142) index complicate things further for here the Scl stars show the opposite of the situation for *S*(3839) – in all metallicity bands the Scl stars lie above the shaded region, and the observed range is larger than the width of the shaded regions.

4.2 C and N abundances via spectrum synthesis of representative Scl stars

In order to quantify and confirm the interpretation of Figs 8 and 10, we have carried spectrum synthesis calculations to determine C and N abundance estimates for a representative subset of the Scl stars in each metallicity group. The 16 stars chosen, which are listed in Table 5, encompass the full range of *S*(3839), *S*(4142), and *W*(*G*) values, as well as [Fe/H], in each metallicity group. In order to perform the synthetic spectrum calculations, however, we need to assume [O/Fe] values for the stars. As indicated in Table 5, we have chosen to assume [O/Fe] = +0.4 for the CN-weak stars and [O/Fe] = 0.0 for the CN-strong stars, the former

value being consistent with GGC first generation and halo field stars and the latter value being consistent with the [O/Fe] values for second-generation stars in GGCs. However, this assumption does not strongly influence the outcome: if instead we employ [O/Fe] = +0.4 for the CN-strong stars, the derived [C/Fe] values are approximately 0.1 dex smaller than for the [O/Fe] = 0.0 case, while the derived [N/Fe] values are ~0.25 dex larger with [O/Fe] = +0.4 compared to the [O/Fe] = 0 case.

The synthetic spectrum calculations were carried as described in Section 4.1.4 and the stellar parameters adopted for each modeled star are given in Table 5. The procedure followed was to first determine the carbon abundance (assuming [O/Fe] = 0.0 or [O/Fe] = +0.4) by minimizing the residuals between the observed and synthetic spectra in the region of the G band of CH ($\lambda \approx 4300 \text{ \AA}$). The nitrogen abundance was determined by considering the comparison of the synthetic and observed spectra in the wavelength interval 3840–3885 Å using the value of [C/Fe] determined from the G band and the assumed oxygen abundance. The process is illustrated in Figs 14 and 15 for the intermediate-metallicity group stars Scl-0492 (CN-weak) and Scl-0247 (CN-strong). The outcome is a difference in [N/Fe] between the two stars of a factor of approximately 4 (CN-strong star has higher [N/Fe]), but the difference in the derived [C/Fe] is essentially zero given the ±0.15 dex uncertainties in the [C/Fe] determination. The derived [C/Fe] and [N/Fe] abundances for the 16 stars analysed are given in Table 5.

The total errors, σ_{total} , in the derived [C/Fe] and [N/Fe] values were calculated as a combination of the errors from uncertainties in the stellar parameters (σ_{SP}) with additional sources of error (σ_{fit}). The quantity σ_{SP} was estimated by repeating the abundance analysis for the star Scl-1490 (assumed to be representative of the sample; see Table 5) varying the atmospheric parameters by $T_{\text{eff}} = \pm 100\text{K}$, $\log g = \pm 0.2$, $[M/H] = \pm 0.4$ and $\xi = \pm 0.2 \text{ km s}^{-1}$. The quantity σ_{fit} comes from the uncertainty in the derived abundances resulting from the comparison of the observed spectrum with model spectra at different abundances. As the derived carbon abundance is dependent on the assumed oxygen abundance, for σ_{fitC} we have added (in quadrature) a further $\sigma_{\text{fit}} = \pm 0.1$ to allow for the uncertainty in adopted oxygen abundances. Similarly, since the determination of the N abundance from the CN features depends on the derived carbon abundance, we have added (in quadrature) to σ_{total} for nitrogen the value of σ_{total} for carbon. Typical values of σ_{total} are 0.16 dex for [C/Fe] and 0.29 dex for [N/Fe].

Our results for [C/Fe] and [N/Fe] are shown in Fig. 16, where we have also plotted the C and N abundance ratios derived by Lardo et al. (2016) for their sample of Scl stars. Unfortunately, we cannot directly compare on a star-by-star basis our results with those of Lardo et al. (2016) because the majority of their observed stars are fainter than ours: there is a small overlap in *V* but there are no stars in common. The two sets of data are in excellent agreement. The upper row shows that for the intermediate and metal-rich groups there is no evidence for an either positive or negative correlation between [C/Fe] and [N/Fe], while an anticorrelation between [N/Fe] and [C/Fe] may be present in the panel for the most metal-poor group, though there is considerable variation in both abundance ratios. This contrasts with the situation for GGCs where a strong anticorrelation between [C/Fe] and [N/Fe] is generally present. The middle row shows that there is a large dispersion in [C/Fe] at all metallicities while the bottom row shows that the largest carbon depletions are generally found in the stars at the highest luminosities. Overall, our synthesis results are consistent with those of Lardo et al. (2016), particularly that there is an intrinsic range in carbon abundance,

Table 7. Observational data for the 45 stars in the Sculptor dSph galaxy observed with GMOS-S and AAOmega. IDs in the form nn_n_nnnn are from Coleman et al. (2005), Scl-nnnn correspond to stars from Walker et al. (2009a), and Sclnn are from Battaglia et al. (2008). Some S(3839) values are missing due to the inter-chip gaps in GMOS-S affecting the spectra. Missing W(NaD) and W(Ba) values result from low S/N for the fainter stars, while missing [Fe/H] values are a consequence of reduced wavelength coverage for fibres at the edges of the AAOmega camera field in the red spectra.

ID	RA J2000	Dec. J2000	V mag	V-I mag	S(3839) mag	S(4142) mag	W(G) Å	W(NaD) Å	W(Ba) Å	[Fe/H] dex
11_1_4953	0:59:28.29	-33:42:07.3	17.013	1.630	0.056	-0.204	7.95	0.805	0.161	-1.44
11_1_5609	0:59:16.93	-33:40:10.6	17.121	1.615	-0.272	-0.380	8.05	0.472	0.215	-2.00
10_8_2607	1:00:16.28	-33:42:37.2	17.127	1.589	0.181	-0.072	13.21	0.715	1.133	-1.39
11_1_6076	0:59:08.59	-33:41:52.7	17.230	1.618	-0.129	-0.266	7.31	0.610	0.196	-1.93
Scl38	1:00:12.76	-33:41:16.0	17.320	1.488	-0.018	-0.240	7.72	0.664	0.174	-2.05
10_8_3291	1:00:06.02	-33:39:39.6	17.350	1.535	0.004	-0.242	8.54	0.773	0.243	-1.96
Scl28	1:00:15.37	-33:39:06.2	17.382	1.536	-	-0.201	7.29	0.559	0.196	-1.84
Scl46	1:00:23.84	-33:42:17.4	17.386	1.512	0.016	-0.225	8.94	0.587	0.234	-1.95
10_8_4149	0:59:52.99	-33:39:18.9	17.454	1.560	-0.051	-0.283	11.66	0.627	0.192	-1.35
Scl17	0:59:56.60	-33:36:41.7	17.522	1.436	-0.092	-0.236	8.44	0.462	0.196	-1.95
11_1_6268	0:59:04.32	-33:44:05.8	17.551	1.437	-0.220	-0.328	8.73	0.569	0.212	-1.80
Scl-0233	0:59:14.56	-33:40:40.0	17.552	1.507	-0.090	-0.319	9.59	0.699	0.172	-1.15
10_8_2179	1:00:22.97	-33:43:02.2	17.559	1.561	-0.064	-0.252	9.61	0.590	0.165	-1.35
Scl-0268	1:00:07.57	-33:37:03.8	17.576	1.420	-0.230	-0.198	8.25	0.486	0.243	-1.69
Scl-0272	1:00:04.62	-33:41:12.0	17.584	1.393	-0.150	-0.296	6.01	0.375	0.131	-2.50
Scl-0248	0:59:40.32	-33:36:06.6	17.585	1.438	-0.195	-0.234	9.17	-	-	-
11_1_6218	0:59:05.35	-33:42:23.8	17.593	1.616	-0.145	-0.237	11.86	0.926	0.240	-0.70
Scl-0784	0:59:47.25	-33:46:30.5	17.598	1.510	-0.053	-0.148	9.82	0.736	0.297	-1.12
11_1_5906	0:59:11.83	-33:41:25.3	17.599	1.425	-0.110	-0.324	7.90	0.462	0.224	-2.02
Scl-0246	0:59:38.11	-33:35:08.1	17.602	1.408	-0.005	-0.235	8.14	-	0.201	-2.36
Scl-0468	1:00:18.29	-33:42:12.2	17.610	1.435	-0.091	-0.250	8.15	0.479	0.206	-1.93
Scl-0247	0:59:37.74	-33:36:00.1	17.632	1.444	0.043	-0.214	9.63	0.504	0.212	-1.70
Scl-0276	1:00:03.59	-33:39:27.1	17.681	1.311	-0.282	-0.344	10.70	0.918	0.244	-1.18
Scl-0492	1:00:28.10	-33:42:34.4	17.684	1.366	-0.215	-0.315	7.54	0.558	0.189	-1.79
Scl-1310	0:59:18.85	-33:42:17.5	17.690	1.460	-0.039	-0.300	9.57	0.680	0.195	-1.57
Scl25	0:59:41.40	-33:38:47.0	17.700	1.447	-	-0.354	10.47	0.643	0.191	-1.48
Scl20	0:59:37.22	-33:37:10.5	17.715	1.500	0.074	-0.337	10.32	0.591	0.350	-1.27
Scl-1490	1:00:07.44	-33:43:19.9	17.720	1.377	-0.235	-0.250	7.23	0.431	0.148	-2.02
Scl-0216	0:59:15.14	-33:42:54.7	17.732	1.389	-0.237	-0.236	8.33	0.466	0.248	-1.42
Scl-1020	0:59:58.25	-33:41:08.6	17.750	1.420	0.203	-0.274	10.10	0.571	0.177	-1.71
Scl-0646	1:00:02.55	-33:48:49.9	17.755	1.382	-	-0.303	7.10	0.590	0.237	-2.05
Scl-0263	0:59:49.21	-33:39:48.9	17.762	1.349	-	-0.296	6.96	0.511	0.145	-2.01
Scl-0470	1:00:17.35	-33:41:08.4	17.784	1.452	-0.009	-0.411	10.42	0.649	0.185	-1.32
Scl-0639	0:59:58.24	-33:45:50.7	17.793	1.409	-0.349	-0.376	9.28	-	-	-
Scl10	0:59:40.46	-33:35:53.8	17.826	1.360	-0.131	-0.310	6.67	0.451	0.194	-2.36
Scl23	0:59:54.47	-33:37:53.4	17.843	1.236	-0.285	-0.357	9.34	0.590	0.198	-1.65
Scl-1036	1:00:39.23	-33:42:12.8	17.852	1.302	-0.195	-0.330	5.05	0.440	0.224	-2.24
Scl24	0:59:57.60	-33:38:32.5	17.872	1.189	-0.146	-0.331	8.68	0.536	0.197	-1.99
Scl-0437	1:00:11.79	-33:42:16.9	17.886	1.449	-0.146	-0.369	10.12	0.534	0.236	-1.24
Scl81	1:00:06.98	-33:47:09.7	17.932	1.343	-0.201	-0.303	7.78	0.691	0.264	-2.07
Scl13	0:59:30.44	-33:36:05.0	18.031	1.260	-0.126	-0.278	6.71	0.396	0.105	-
Scl74	1:00:05.93	-33:45:56.5	18.041	1.291	-0.220	-0.245	6.27	-	-	-
Scl59	1:00:17.36	-33:43:59.6	18.054	1.319	-0.053	-0.272	6.88	0.354	0.196	-2.13
Scl54	1:00:15.18	-33:43:11.0	18.087	1.397	0.031	-0.285	10.07	0.647	0.192	-1.41
Scl49	0:59:08.60	-33:42:29.4	18.113	1.219	-0.214	-0.280	6.22	-	-	-

Note. (a) This star is the CEMP-s star discussed in Salgado et al. (2016). In that paper the [Fe/H] value of -1.0 from Geisler et al. (2005) was adopted.

which is present at all metallicities and which cannot be entirely explained by evolutionary mixing effects.

4.3 Sodium

Determinations of the sodium abundance in GGCs, and its star-to-star variation, stem principally from the analysis of high dispersion spectra, which allow the measurement of relatively weak Na lines. Such high dispersion spectra generally also allow the measurement of abundances for oxygen, and thus investigation of the extent of

the Na/O anticorrelation (e.g. Carretta et al. 2009; Carretta 2016). Indeed the Na/O anticorrelation is one of the key features of the GGC light element abundance anomaly phenomenon. Here we adopt a different approach in that we use the strengths of the Na D lines in intermediate resolution spectra as a measure of sodium abundance, and then seek evidence for a Na/N correlation using the CN-band strengths as an indicator of the N abundance. Since in GGCs the stars that are depleted in oxygen are enhanced in N, investigating a Na/CN correlation is equivalent to exploring the Na/O anticorrelation. This is not a new approach – earlier studies

Table 8. Observational data for the 108 stars in the Sculptor dSph galaxy observed only with AAOmega. IDs use the same nomenclature as in Table 7. Missing W(NaD) and W(Ba) values result from low S/N for the fainter stars, while missing [Fe/H] values are a consequence of reduced wavelength coverage for fibres at the edges of the AAOmega camera field in the red spectra.

ID	RA J2000	Dec J2000	V mag	V-I mag	W(NaD) Å	W(Ba) Å	[Fe/H] dex
6.6.0152	01:01:14.53	-33:30:09.2	16.862	1.587	0.782	0.298	-1.712
Sci04	00:59:55.63	-33:33:24.6	16.890	1.297	0.613	0.197	-2.406
10.8.0644	01:01:02.87	-33:38:52.2	17.033	1.562	0.686	0.194	-2.077
11.1.6226	00:59:04.80	-33:38:44.2	17.046	1.704	0.880	0.223	-1.617
6.3.0197	01:02:22.18	-33:23:04.4	17.108	1.482	0.690	-	-2.355
Sci92	01:00:25.30	-33:50:50.8	17.109	1.159	0.962	0.202	-0.671
10.7.0022	01:01:49.38	-33:54:09.9	17.130	1.507	0.444	0.145	-2.602
11.2.0504	00:59:43.15	-33:56:46.7	17.130	1.550	0.533	0.194	-2.254
10.8.1013	01:00:49.36	-33:42:00.5	17.137	1.587	0.663	0.197	-2.116
6.5.0546	01:00:42.55	-33:35:47.3	17.164	1.496	0.624	0.182	-1.780
10.1.1614	01:02:23.58	-33:43:43.8	17.184	1.547	0.460	0.205	-2.323
11.1.7127	00:58:42.58	-33:48:33.4	17.189	1.576	0.721	0.215	-1.976
Sci27	01:00:34.04	-33:39:04.6	17.200	1.701	0.727	0.267	-1.346
11.7.0120	00:57:55.06	-33:59:40.9	17.201	1.449	0.709	0.224	-2.304
Sci84	01:00:38.12	-33:48:16.9	17.212	1.482	0.582	0.177	-2.054
Sci70	01:00:50.87	-33:45:05.2	17.213	1.673	0.678	0.204	-1.568
10.8.0128	01:01:39.62	-33:45:04.3	17.222	1.604	0.541	0.234	-1.807
7.2.0287	00:58:45.46	-33:10:00.4	17.223	1.477	0.640	0.304	-1.383
7.6.0038	00:58:15.72	-33:27:16.2	17.226	1.454	0.711	0.188	-1.943
11.1.4989	00:59:27.68	-33:40:35.6	17.229	1.475	0.556	0.166	-2.163
Sci77	00:59:55.68	-33:46:40.1	17.233	1.388	0.690	0.191	-2.179
6.5.0027	01:01:49.33	-33:36:23.9	17.233	1.505	0.582	0.216	-1.623
11.8.0435	00:56:46.94	-33:48:20.6	17.235	1.480	-	-	-2.048
10.8.0856	01:00:54.17	-33:40:14.6	17.257	1.538	0.647	0.282	-1.843
10.3.0033	01:03:53.61	-34:13:47.9	17.261	1.614	0.691	0.165	-2.177
Sci76	00:59:12.09	-33:46:20.8	17.266	1.386	0.561	0.152	-2.004
11.1.5108	00:59:26.25	-33:46:52.9	17.272	1.541	0.679	0.111	-1.899
10.8.1236	01:00:42.48	-33:44:23.4	17.273	1.581	0.956	0.217	-1.595
Sci39	00:59:46.41	-33:41:23.5	17.304	1.605	0.902	0.221	-0.956
11.1.5411	00:59:20.80	-33:44:04.9	17.309	1.470	0.555	0.204	-2.269
11.1.4528	00:59:35.36	-33:44:09.4	17.369	1.672	0.859	0.288	-1.220
11.5.0233	00:57:33.46	-34:24:47.7	17.373	1.364	0.707	0.200	-2.115
10.7.0734	01:00:18.31	-33:53:31.5	17.399	1.487	0.595	-	-1.897
6.5.1071	01:00:17.76	-33:35:59.6	17.400	1.549	0.819	0.247	-1.289
6.5.0436	01:00:50.23	-33:36:38.2	17.412	1.403	0.609	0.151	-2.147
6.6.0203	01:00:54.64	-33:25:23.0	17.424	1.503	0.620	0.160	-1.826
7.5.0227	00:57:32.70	-33:34:06.9	17.428	1.362	0.586	0.141	-1.992
6.5.0153	01:01:21.65	-33:36:19.5	17.470	1.326	0.502	0.117	-2.667
6.6.0338	01:00:18.20	-33:31:40.4	17.473	1.597	0.752	0.223	-1.467
10.7.0487	01:00:45.63	-34:01:27.5	17.480	1.430	0.538	0.322	-2.202
10.8.2693	01:00:14.82	-33:44:22.1	17.481	1.468	0.560	0.148	-2.009
Sci09	01:00:20.29	-33:35:34.5	17.495	1.409	0.561	-	-2.085
10.7.0815	01:00:10.92	-34:01:34.8	17.496	1.386	0.488	0.142	-2.179
Sci88	01:00:00.49	-33:49:35.8	17.512	1.365	0.466	0.142	-2.556
10.7.0891	01:00:04.20	-33:52:21.8	17.525	1.364	0.437	0.096	-2.544
11.1.7421	00:58:33.76	-33:43:18.6	17.525	1.449	0.665	0.264	-1.888
11.1.5592	00:59:17.78	-33:46:01.7	17.526	1.466	0.501	0.184	-1.715
11.1.5483	00:59:19.15	-33:38:51.0	17.546	1.415	0.566	-	-1.779
Sci-0259	00:59:54.20	-33:40:27.0	17.560	1.520	0.743	-	-1.506
Sci-0665	01:00:44.27	-33:49:18.8	17.570	1.480	0.561	0.177	-1.565
Sci-0993	01:00:08.98	-33:50:22.9	17.590	1.370	0.664	0.209	-2.034
11.2.0913	00:58:46.71	-33:53:36.8	17.592	1.375	0.598	0.270	-1.828
Sci-0782	00:59:39.48	-33:45:39.2	17.610	1.410	0.432	-	-1.537
10.1.0634	01:03:18.66	-33:47:15.8	17.622	1.506	0.560	0.203	-1.846
Sci-0108	01:01:19.27	-33:45:41.6	17.630	1.420	0.532	0.221	-1.992
Sci-0968	00:59:14.37	-33:31:43.8	17.640	1.340	0.536	0.223	-1.583
Sci-1183	00:59:42.57	-33:42:18.2	17.650	1.500	0.543	0.202	-1.257
Sci-0822	00:59:44.11	-33:28:11.7	17.680	1.360	0.593	0.273	-1.449
7.4.1809	00:59:47.21	-33:33:37.0	17.680	1.336	0.508	0.186	-2.198
Sci-0674	01:00:48.22	-33:49:55.5	17.720	1.400	0.659	-	-2.298
Sci-0636	01:00:53.68	-33:52:27.4	17.720	1.380	0.490	0.109	-1.904
Sci-0772	00:59:46.15	-33:48:39.1	17.720	1.440	0.813	0.264	-

Table 8 – *continued*

ID	RA J2000	Dec J2000	V mag	V-I mag	W(NaD) Å	W(Ba) Å	[Fe/H] dex
10.2.0586	01:02:08.04	−33:57:50.4	17.732	1.392	0.542	0.108	−1.833
11.2.0748	00:59:13.96	−34:00:38.5	17.737	1.292	0.570	0.313	−2.168
Scl-0667	01:00:29.22	−33:55:44.2	17.740	1.400	0.619	0.149	−1.709
Scl-1281	00:59:36.98	−33:30:28.3	17.740	1.310	0.621	–	−1.679
Scl-0649	01:00:18.96	−33:45:14.7	17.750	1.300	0.571	0.200	−2.084
Scl-0242	00:59:37.77	−33:41:15.4	17.750	1.370	0.636	0.160	−1.745
Scl-0454	01:00:25.78	−33:30:25.4	17.760	1.320	0.463	0.212	−2.133
Scl-0655	01:00:21.11	−33:56:27.9	17.770	1.320	0.425	–	−2.258
Scl-0892	01:01:45.19	−33:25:40.1	17.770	1.300	0.673	0.205	−2.287
Scl-0847	01:00:38.91	−33:26:09.6	17.780	1.350	0.842	–	−2.216
Scl-0095	01:01:15.09	−33:42:41.8	17.780	1.350	0.867	–	−2.074
Scl-0790	00:59:48.16	−33:50:22.7	17.790	1.420	0.717	0.238	−0.722
Scl-0947	00:58:38.77	−33:35:02.3	17.800	1.300	0.609	0.192	−2.253
Scl50	00:59:47.05	−33:42:54.2	17.810	1.389	0.586	0.281	−1.541
Scl-0472	01:00:27.01	−33:38:22.0	17.820	1.420	0.621	–	−1.609
Scl89	01:00:10.49	−33:49:36.9	17.829	1.296	0.524	0.137	−1.909
Scl-0099	01:00:48.54	−33:40:52.7	17.830	1.420	0.770	–	−1.484
10.1.2031	01:01:59.91	−33:51:12.9	17.861	1.407	0.639	–	−1.865
Scl-0653	01:00:24.62	−33:44:28.9	17.870	1.340	0.617	–	−1.772
Scl-0804	01:01:30.79	−33:57:29.9	17.870	1.340	0.691	–	−2.524
Scl-0456	01:00:26.19	−33:31:38.8	17.870	1.300	0.529	0.146	−2.180
Scl-0785	00:59:47.66	−33:47:29.4	17.880	1.460	0.561	0.194	−1.315
Scl-0874	00:58:04.07	−33:50:41.8	17.880	1.380	0.615	0.111	−2.025
Scl-0482	01:00:37.78	−33:44:08.7	17.880	1.340	0.566	0.228	−2.008
Scl-0657	01:00:33.85	−33:44:54.4	17.890	1.340	0.445	–	−1.822
Scl-0289	00:58:46.95	−33:38:53.5	17.890	1.350	0.608	0.201	−2.098
Scl-0522	01:02:25.28	−33:39:50.0	17.890	1.310	0.572	0.216	−2.228
Scl-1140	01:00:11.73	−33:44:50.3	17.900	1.320	0.313	0.126	−2.461
Scl-0683	01:00:01.44	−33:51:16.7	17.900	1.290	–	–	−1.731
Scl80	01:00:42.96	−33:47:06.4	17.907	1.138	0.533	0.178	−2.552
Scl-1034	01:00:45.42	−33:52:14.7	17.910	1.260	0.717	0.441	−1.523
Scl-1321	00:59:49.90	−33:44:05.0	17.910	1.340	0.616	0.164	−1.610
Scl-0509	01:02:18.74	−33:36:15.3	17.910	1.250	–	–	−2.474
Scl-1054	00:57:35.52	−33:41:21.9	17.940	1.320	0.754	0.198	−1.780
Scl-0264	00:59:59.09	−33:36:44.9	17.950	1.280	0.539	0.142	−2.489
Scl-0106	01:01:10.27	−33:38:37.8	17.950	1.250	0.607	0.101	−2.109
Scl-0669	01:00:46.51	−33:46:47.1	17.960	1.300	0.568	0.171	−2.568
Scl-0668	01:00:34.32	−33:49:52.8	17.960	1.420	0.693	0.159	−1.286
Scl-0787	00:59:44.04	−33:49:41.1	17.960	1.370	0.960	0.272	−1.420
Scl-1287	00:59:37.61	−33:40:22.0	17.960	1.330	0.521	–	−2.037
Scl-0223	00:59:11.34	−33:37:28.2	17.980	1.330	0.607	0.130	−1.668
Scl-0476	01:00:32.83	−33:36:07.4	17.980	1.280	0.422	0.169	−1.919
Scl26	00:59:30.49	−33:39:04.0	17.981	1.252	0.527	0.200	−2.094
Scl07	00:59:58.31	−33:34:40.4	17.983	1.283	0.583	0.233	−1.347
Scl-0890	01:01:00.91	−33:27:54.9	17.990	1.310	0.492	–	−1.828
Scl-0835	01:00:02.68	−33:30:25.1	18.000	1.310	0.502	0.162	–

have shown that the strengths of the Na D lines are stronger in CN-strong GGC red giants compared to CN-weak stars (Cottrell & Da Costa 1981; Da Costa 1981; Norris & Pilachowski 1985).

As regards Scl, the investigation of the existence of any relation between CN-band and Na D line strengths is vital: CN-band variations on their own are not sufficient evidence for the presence of GGC-like abundance anomalies as they may result from variable amounts of evolutionary mixing on the giant branch. A direct connection between the CN-band and Na D line strengths, on the other hand, would be strong evidence in favour of the occurrence of the GGC abundance anomaly phenomenon in this dSph.

As a first step, we have determined the equivalent widths, denoted by $W(\text{NaD})$, of the Na D lines in the spectra of the RGB stars in our

set of comparison GGC, using the approach outlined in Section 2.1. For both NGC 288 and NGC 6752, the cluster radial velocity is not sufficient to allow a clear separation of the stellar Na D lines from any interstellar component, assumed to have a velocity near zero, at the resolution of the red spectra. However, the reddenings for these clusters are low (Harris 1996) (see Table 2) so that any interstellar contribution to the measured Na D line strengths in the cluster red giant spectra can be assumed to be negligible. This is not the case for the cluster M55, which is both more metal-poor and more highly reddened than NGC 288 and NGC 6752. Fortunately, the radial velocity of this cluster is sufficiently high that the stellar and interstellar Na D lines are clearly separated in the M55 red giant spectra, allowing unambiguous measurement of the stellar lines.

The results are shown in Fig. 17, where, particularly for the more metal-rich clusters, it is apparent that the CN-strong stars, as anticipated, generally have larger $W(\text{NaD})$ values than the CN-weak stars of similar luminosity. The typical error in the $W(\text{NaD})$ values was calculated in the same way as for the indices discussed in Section 4. Specifically, for GGCs stars, we use the rms from a fit to the CN-weak population in the $(W(\text{NaD}), V - V_{\text{HB}})$ plane. This yields typical errors for the GGC $W(\text{NaD})$ values of 0.11 Å, 0.12 Å, and 0.12 Å for the clusters NGC 288, NGC 6752, and M55, respectively. We have then used synthetic spectra calculations to estimate the extent of the variations in $[\text{Na}/\text{Fe}]$ present in our GGC spectra. The procedure was similar to that used in the Section 4.1.4: we calculated synthetic spectra for a number of $(T_{\text{eff}}, \log g)$ pairs appropriate to the cluster RGBs and with different values of $[\text{Na}/\text{Fe}]$. Based on the results of Carretta et al. (2009) and Carretta (2016) for example, we assumed a range of ~ 0.5 dex in $[\text{Na}/\text{Fe}]$ as encompassing the extent of the $[\text{Na}/\text{Fe}]$ variations present in the GGCs. The synthetic spectra were smoothed to the observed resolution and the corresponding Na D strengths determined. The results are shown as the shaded bands in Fig. 17, where the upper boundary represents the higher value of $[\text{Na}/\text{Fe}]$ adopted and the lower boundary the reverse. The actual values of the upper and lower $[\text{Na}/\text{Fe}]$ limits employed for each cluster are given in the upper section of Table 6. These values were determined by ensuring that the corresponding shaded regions in Fig. 17 matched the location of the GGC stars. For example, the limits on $[\text{Na}/\text{Fe}]$ employed for NGC 288 and NGC 6752 are -0.1 and 0.4 , and 0.1 and 0.6 dex, respectively, values that are entirely consistent with those based on high dispersion spectroscopy (Carretta et al. 2009) where the full range for the observed $[\text{Na}/\text{Fe}]$ values in the NGC 288 sample is $0.05 \leq [\text{Na}/\text{Fe}] \leq \sim 0.7$ dex and is $0.1 \leq [\text{Na}/\text{Fe}] \leq \sim 0.75$ dex for NGC 6752 sample. In the case of M 55, Carretta et al. (2009) give a range $0.1 \leq [\text{Na}/\text{Fe}] \leq \sim 0.7$ dex while our estimation reveals a similar range but at a lower overall $[\text{Na}/\text{Fe}]$: -0.5 to 0.0 dex.

For the Scl stars we followed a similar procedure, retaining the same metallicity groups as first discussed in Section 3. In particular, we note that the radial velocity of Scl is sufficiently large that any interstellar component would be distinguished from the stellar lines, but in fact we see little evidence for any interstellar component in the Scl spectra consistent with the low foreground reddening. The measured $W(\text{NaD})$ for the Scl giants for which we have blue spectra are shown in the panels of Fig. 17, with the CN-strong stars (see middle row panels of Fig. 8) plotted as black-filled circles and CN-weak stars as black open circles. Red spectra are available for a substantially larger number of Scl members than those with blue spectra, and we show the $W(\text{NaD})$ values for these additional stars as grey x-signs in Fig. 17. The typical error for the Scl $W(\text{NaD})$ values is given, as before, by the standard deviation of the differences between measurements on the two sets of spectra, scaled by $\sqrt{2}$. Considering first the stars for which a CN-classification is possible, it is clear that, unlike the situation for the GGC stars, there is no indication that the CN-strong Scl stars have preferentially larger $W(\text{NaD})$ values than their CN-weak counterparts. The possible exception is in the most-metal poor panel where the two most luminous CN-strong stars have somewhat larger $W(\text{NaD})$ values than the CN-weak stars at similar $V - V_{\text{HB}}$, although these stars are not obviously distinguished when considering the full Scl sample in this metallicity group. We caution, however, that at the lowest metallicities the relative uncertainty in the $W(\text{NaD})$ measurements is comparable to the size of the apparent excess in $W(\text{NaD})$. Overall, our results strongly imply that the GGC light element abundance anomaly is not prevalent in Scl, a result that is consistent with those

from high dispersion spectroscopy that looked explicitly for the O/Na anticorrelation in Scl, and that did not find any support for its existence (e.g. Geisler et al. 2005). Norris et al. (2017) reached the same conclusion for the Carina dSph.

Two other effects are also immediately evident from Fig. 17. First, whether considering just the Scl stars with blue spectra or the entire sample, the median $W(\text{NaD})$ for the Scl stars is significantly lower than for the GGC comparison stars, even allowing for the incomplete overlap in luminosity. The offset is particularly marked for the intermediate-metallicity stars in the middle panel, but it is also present in the upper panel. It is less marked in the lowest abundance panel but again the $W(\text{NaD})$ values are least certain for this Scl group. Second, considering the full sample of Scl stars, there are a small number that have $W(\text{NaD})$ values significantly larger than the bulk of the population, and such stars appear present in all three metallicity groups. This would suggest that there are some Scl stars that have larger $[\text{Na}/\text{Fe}]$ values than the majority of stars with similar metallicities.

To investigate these effects, we have again used synthetic spectrum calculations as for the GGC stars. The pink-shaded regions in Fig. 17 show the range in $W(\text{NaD})$ values for a range in $[\text{Na}/\text{Fe}]$ of 0.5 dex, as for the GGCs. However, in the Scl case, at least for the two more metal-rich groups, the $[\text{Na}/\text{Fe}]$ limits are required to be at least ~ 0.6 dex lower than the corresponding values for the GGC stars in order to reproduce the Scl line strengths. This is less obviously the case for the most metal-poor group of Scl stars. Here, the majority of Scl stars again have weaker Na D line strengths than would be inferred from extrapolating the GGC M55 data, but the synthetic spectrum predictions for the same $[\text{Na}/\text{Fe}]$ range as for the two more metal-rich groups do not encompass the Scl $W(\text{NaD})$ values. Whether this is a result of the larger relative uncertainty in the Scl $W(\text{NaD})$ values at low $[\text{Fe}/\text{H}]$, or an unknown systematic effect is unclear but, interpreted literally, the data would suggest both that the range in $[\text{Na}/\text{Fe}]$ for these Scl stars is larger than the 0.5 dex used in the synthetic spectra calculations, and that the typical value of $[\text{Na}/\text{Fe}]$ is higher than that for the two more metal-rich groups.

Overall, the relative weakness of the Scl Na D line strengths compared to the GGC stars at all metallicities is an outcome consistent with the high dispersion spectroscopic results of Shetrone et al. (2003) and Geisler et al. (2005). They find sub-solar values of $[\text{Na}/\text{Fe}]$ for Scl red giants: typically $[\text{Na}/\text{Fe}] \approx -0.55$, in marked contrast to (first generation) GGC stars which have $[\text{Na}/\text{Fe}] \approx 0.1$ dex. Shetrone et al. (2003) have found similar depletions relative to solar values for $[\text{Na}/\text{Fe}]$ in other dSphs (Carina, Fornax, Leo I), while the extensive study of Carina red giants of Norris et al. (2017) finds $\langle [\text{Na}/\text{Fe}] \rangle = -0.28 \pm 0.04$ dex and notes that this is significantly below the typical $[\text{Na}/\text{Fe}] \approx 0.0$ in Galactic halo (and GGC first generation) stars. Letarte et al. (2010) and Lemasle et al. (2014) have shown that this is also the case in the Fornax dSph.

We now consider the panels of Fig. 17 in more detail as regards the Scl stars. In the top panel there is no clear separation between the Scl CN-strong and CN-weak stars and the majority of the Scl points in the full sample fall within or close to the pink band. Indeed for the majority of the Scl stars the dispersion in the $W(\text{NaD})$ values is consistent with a single $[\text{Na}/\text{Fe}]$ value of order $[\text{Na}/\text{Fe}] = -0.7$. There are, however, a small number of Scl stars that lie at $W(\text{NaD})$ values substantially above the majority of the data points. There are two possible reasons for this: larger than average $[\text{Na}/\text{Fe}]$ values or higher than average $[\text{Fe}/\text{H}]$ values leading to a higher $W(\text{NaD})$ value. As an example, in this panel there are two CN-weak

stars that lie significantly above ($\sim 5\sigma$) the pink-shaded region. These stars are 11_1.6218 and Scl-0276 and their metallicities as determined here are $[\text{Fe}/\text{H}] = -0.70$ and -1.18 , respectively. While these stars are among the most metal-rich in the group, higher metallicity cannot be the entire explanation of the larger $W(\text{NaD})$ as stars Scl-0233 and Scl-0784 have similar $V - V_{\text{HB}}$ values, and similar metallicities ($[\text{Fe}/\text{H}] = -1.15$ and -1.12 , respectively), yet their $W(\text{NaD})$ values place them close to or within the pink-shaded regions. There are six other stars in the full sample for this metallicity group that show similarly strong $W(\text{NaD})$ values: Scl-0787, 6_5_1071, 11_1_4528, Scl39, 10_8_1236, and Scl92, and their metallicities range from $[\text{Fe}/\text{H}] = -1.59$ to -0.67 dex, which encompasses the full range of metallicities in the Scl metal-rich group. While high dispersion follow-up is needed for confirmation, as an indication of the increased $[\text{Na}/\text{Fe}]$ required, we show in the top panel of Fig. 17, as a green-dashed line, the locus for the solar value of $[\text{Na}/\text{Fe}]$ at $[\text{Fe}/\text{H}] = -1.25$ dex. Its location suggests that a minority population among the Scl metal-rich stars may have substantially higher, by perhaps 0.5 dex, $[\text{Na}/\text{Fe}]$ values compared to those for the bulk of the population.

Turning now to the middle panel of Fig. 17, the most remarkable characteristic is again the notably weaker $W(\text{NaD})$ values for the Scl stars compared to those for the GGC NGC 6752. The spectrum synthesis calculations suggest that this difference requires $[\text{Na}/\text{Fe}]$ for the Scl stars to be 0.6–0.8 dex lower than the value for the CN-weak stars in the GGC NGC 6752. As noted above, such a difference in $[\text{Na}/\text{Fe}]$ between the Scl stars and the CN-weak (first generation) GGC stars is consistent with the results of the high dispersion studies of Shetrone et al. (2003) and Geisler et al. (2005). We note also, given the uncertainty in the $W(\text{NaD})$ values, that there is no requirement for the presence of a spread in $[\text{Na}/\text{Fe}]$ in this sample of Scl stars.

As discussed above, the location of the Scl stars in the bottom panel of Fig. 17 relative to the pink band suggests for these more metal-poor stars a higher overall $[\text{Na}/\text{Fe}]$ ratio, and potentially larger range in $[\text{Na}/\text{Fe}]$, compared to the two more metal-rich Scl groups. We caution against placing too much weight on this outcome, given that the uncertainty in the $W(\text{NaD})$ values for these stars is an appreciable fraction of the measured values. We note, in particular, that the two Scl giants with largest $W(\text{NaD})$ values in this panel are stars Scl-0847 and Scl-0095. They have virtually identical locations in the panel at $(V - V_{\text{HB}}) \approx -2.6$ and $W(\text{NaD}) \approx 0.85$ Å and their metallicities are $[\text{Fe}/\text{H}] = -2.21$ and $[\text{Fe}/\text{H}] = -2.07$, respectively.

In summary, we conclude that the study of Scl $W(\text{NaD})$ line strengths in our large sample of Scl giants, as discussed in this section, reveals three results. First, that there is no evidence to support any connection between CN-strength and enhanced $W(\text{NaD})$ as is seen in the GGC stars. Second, the majority of Scl stars have weaker $W(\text{NaD})$ strengths than the GGC stars at comparable luminosities, consistent with $[\text{Na}/\text{Fe}]$ values for the Scl giants that are ~ 0.6 dex lower than the approximately solar $[\text{Na}/\text{Fe}]$ values for the GGC first-generation stars (and the halo field in general). Both of these results are consistent with earlier high dispersion spectroscopic samples of small samples of Scl giants (Shetrone et al. 2003; Geisler et al. 2005). Third, we have found indications of the existence of a minority population (~ 5 per cent) of Scl giants that appear to have significantly higher $[\text{Na}/\text{Fe}]$ values compared to the majority: high dispersion spectroscopy of these stars is required to confirm our results and to ascertain whether any other elements also show differences from the population norm.

5 SUMMARY AND CONCLUSION

In this work we have analysed intermediate resolution blue and red spectra of an extensive sample of red giants in the Scl dwarf spheroidal galaxy in order to investigate whether there is evidence for the existence in Scl of the light-element abundance variations that are well established in GGCs. As part of the analysis we have also employed similar spectra of red giants in a number of GGCs as comparator objects. We have used the red spectra, which originate from the AAT/AAOmega instrument, to generate individual metallicity estimates for the Scl stars using a line-strength calibration derived from the GGC spectra. We find that our Scl metallicity estimates are in good accord with existing determinations for the stars in common. This enabled us to split the Scl sample into three metallicity groups: low, intermediate, and high, each of which has a comparator GGC: M55, NGC 6752, and NGC 288, respectively.

We then measured, on blue spectra for the Scl stars that are from Gemini GMOS-S observations, the CN-band strength indices $S(3839)$ and $S(4142)$, as well as the CH-band strength index $W(G)$. Similarly, indices were determined from the AAOmega blue spectra for the GGC comparison stars. In addition, we measured the strength of the sodium D-lines, denoted by $W(\text{NaD})$, on the AAOmega red spectra of both the Scl and GGC stars. Analysis of the GGC-star line and band-strength indices generated results in accord with expectations, given the established existence of the light-element abundance variations in the comparison GGCs. Specifically, as is evident in Figs 6 and 7, the distribution of the CN-band strength index $S(3839)$ in each cluster is bimodal, allowing classification of stars as ‘CN-weak’ or ‘CN-strong’.

The CN-strong GGC-stars generally have lower values of the CH-band strength index $W(G)$ and, consequently, the differential indices $\delta S3839$ and $\delta W(G)$ are found to be anticorrelated. The CN-strong stars also have larger values of the sodium line-strength index $W(\text{NaD})$ compared to CN-weak stars of similar luminosity. These results are consistent with the standard interpretation that the CN-strong stars have higher nitrogen and sodium abundances, and lower carbon abundances, compared to the CN-weak stars. Spectrum synthesis calculations confirm this interpretation – the CN-strong and CN-weak index values are consistent with abundance differences of $\Delta[\text{N}/\text{Fe}] \approx +1.0$ and $\Delta[\text{C}/\text{Fe}] \approx -0.5$ for an assumed $\Delta[\text{O}/\text{Fe}] \approx -0.4$ dex (see Fig. 6 and Table 4). Moreover, spectrum synthesis supports an abundance difference $\Delta[\text{Na}/\text{Fe}] \approx 0.5$ dex between the two populations, consistent with the range of $[\text{Na}/\text{Fe}]$ values seen in these clusters based on high dispersion spectroscopy (e.g. Carretta et al. 2009).

The situation for the Scl stars, however, is more complex, yet there is little evidence to support the existence of similar correlated abundance differences to those seen in the GGCs. This is consistent with the results of Geisler et al. (2005), who showed from high-dispersion spectra that a small sample of Scl giants lacked the O–Na anticorrelation that is one of the characteristic signatures of the GGC light-element abundance variations phenomenon. Norris et al. (2017) reached a similar conclusion for the Carina dSph. Nevertheless, variations in the CN- and CH-band strength indices are present in our Scl sample, although within each metallicity group there is no evidence that this variation is driven by variations in $[\text{Fe}/\text{H}]$; see Fig. 11. We also find, in contrast to the negative correlations seen for the GGCs, that the differential indices $\delta S3839$ and $\delta W(G)$ are positively (for the two metal-poorer groups) or uncorrelated (metal-rich group) for the Scl stars. An analogous analysis of the $\delta S3839$ and δCH indices for Scl stars given in Lardo

et al. (2016) generates a very similar result. The overall range in the indices is comparable with, or perhaps larger than, the range seen for the corresponding GGCs. This suggests that the range in [N/Fe] and [C/Fe] values in the Scl is similar to those in the GGCs. However, in each metallicity case, the *S*(3839) and *W*(*G*) values are below the values for the GGC stars. Given that the Scl stars all lie near the RGB-tip, this difference may be the result of larger C-depletions from evolutionary mixing. Overall, such an interpretation is consistent with both the spectrum synthesis analysis of a representative subsample of our stars, for which our [C/Fe] and [N/Fe] abundances are in excellent accord with those of Lardo et al. (2016), and their interpretation that [C/Fe] decreases with increasing luminosity on the Scl RGB at all metallicities, and that there is evidence for a significant dispersion in [C/Fe] at given [Fe/H] among the Scl stars.

As regards sodium in the Scl stars, the strongest result is the indication that the Scl stars have significantly lower [Na/Fe] values, by order of 0.5 dex, compared to the CN-weak GGC stars, i.e. the first-generation GGC stars whose abundance ratios are similar to those for field halo stars at similar metallicity. This result has been seen before in dSph galaxies: Shetrone et al. (2003) and Geisler et al. (2005) revealed the [Na/Fe] deficiency in Scl based on high dispersion spectra of a small sample of Scl giants. Further, Norris et al. (2017) have shown that the same situation applies in Carina, and the extensive studies of Letarte et al. (2010) and Lemasle et al. (2014) show that this is also the case in the Fornax dSph. Similarly, Hasselquist et al. (2017) have used near-IR APOGEE spectra to study in detail the abundance patterns in a large sample of stars in the Sgr dSph. While the sample is dominated by relatively metal-rich stars in the Sgr core, a deficiency in [Na/Fe] of size ~ 0.4 dex compared to Milky Way stars of similar [Fe/H] values is evident. Hasselquist et al. (2017) (see also McWilliam, Wallerstein & Mottini 2013, and the references therein) argue that the deficiency in [Na/Fe], along with the overall abundance patterns in their Sgr sample, suggests that the initial mass function for the star formation in Sgr was ‘top-light’, i.e. relatively lacking in massive stars that are the primary nucleosynthetic source for sodium. This may also be the explanation for the relative deficiency in [Na/Fe] in Scl and the other dSphs. Intriguingly, we do see evidence for a small population (~ 5 per cent) of Scl giants that appear to have notably higher [Na/Fe] ratios than the bulk of the Scl population. Such a population is not evident in the Carina sample of Norris et al. (2017) but inspection of fig. 6 of Hasselquist et al. (2017) suggests that there are also a small number of Sgr giants (at lower [Fe/H] than the bulk of the sample) that have relatively high [Na/Fe] values. Such stars, and the objects in Scl, deserve further attention.

In conclusion, our principal result is that the typical signatures of the GGC light element abundance anomalies are not present in our Sculptor data set, indicating that the dSph star formation environment must be fundamentally different to that which gives rise to the multiple populations in GGCs. For completeness, we note that the Milky Way halo (as distinct from the Bulge; Schiavon et al. 2016a) has small population (~ 3 per cent) of stars with CN/CH indices like those for GGCs stars (Martell et al. 2011). With our sample size, we cannot rule a similar frequency of such stars in Scl, but there is no evidence that Scl has possessed a globular cluster whose dissolution would be the origin of such stars, in the same way as is hypothesized for the halo field objects. Lardo et al. (2016) reached a similar conclusion.

There are two fundamental differences between the Scl dSph and the comparison GGCs that may be relevant as to why the light element abundance anomalies are seen in the GGCs and not in

Scl and other dSphs. The first is that the Scl dSph is dark matter dominated (e.g. Walker et al. 2009b), while GGCs are generally considered dark-matter free. The second difference is structural in the sense that length scales, e.g. half-mass radii, are substantially larger in dSphs than for GGCs, and correspondingly, the central densities are much higher in GGCs than in dSphs. Given these differences, it is probable that GGCs form at the centres of large star-forming complexes and with high SF rates, while dSphs like Scl are likely the result of independent evolution within a dark-matter halo with relatively low star-formation rates. While the actual mechanism generating the light element abundance anomalies remains unknown, it would seem that high stellar density and high star formation efficiency at formation are essential requirements. Exploration of the presence or absence of the exact same GGC light element abundance anomalies in the SMC 6–8 Gyr old clusters (Hollyhead et al. 2016, 2018) is therefore a vital task, as these clusters effectively differ only in age from the GGC. A definitive outcome would decide, for example, whether ‘special conditions at the earliest epochs’ are required or not.

ACKNOWLEDGEMENTS

This study is based, in part, on observations (Program GS-2012B-Q-5) obtained at the Gemini Observatory, which is operated by the Association of Universities for Research in Astronomy, Inc., under a cooperative agreement with the NSF on behalf of the Gemini partnership: the National Science Foundation (United States), the National Research Council (Canada), CONICYT (Chile), Ministerio de Ciencia, Tecnología e Innovación Productiva (Argentina), and Ministério da Ciência, Tecnologia e Inovação (Brazil). CS acknowledges support provided by CONICYT, Chile, through its scholarships program CONICYT-BCH/Doctorado Extranjero 2013-72140033. This research has been supported in part by the Australian Research Council through Discovery Projects grants DP120101237, DP150103294, and FT140100554.

REFERENCES

- Alonso A., Arribas S., Martínez-Roger C., 1999, *A&AS*, 140, 261
Aoki W. et al., 2009, *A&A*, 502, 569
Bastian N., Lardo C., 2018, *ARA&A*, 56
Battaglia G., Irwin M., Tolstoy E., Hill V., Helmi A., Letarte B., Jablonka P., 2008, *MNRAS*, 383, 183
Cannon R., Croke B., Bell R., Hesser J., Stathakis R., 1998, *MNRAS*, 298, 601
Carretta E., 2016, preprint ([arXiv:1611.04728](https://arxiv.org/abs/1611.04728))
Carretta E., Gratton R., Lucatello S., Bragaglia A., Bonifacio P., 2005, *A&A*, 433, 597
Carretta E., Bragaglia A., Gratton R., Lucatello S., 2009, *A&A*, 505, 139
Carretta E., Bragaglia A., Gratton R., Recio-Blanco A., Lucatello S., D’Orazi V., Cassisi S., 2010, *A&A*, 516, A55
Castelli F., Kurucz R., 2003, in IAU Symp. 210, Modelling of Stellar Atmospheres, Cambridge Univ. Press, Cambridge, p. 20
Coleman M. G., Da Costa G., Bland-Hawthorn J., 2005, *AJ*, 130, 1065
Cottrell P., Da Costa G., 1981, *ApJ*, 245, L79
D’Antona F., Gratton R., Chieffi A., 1983, *Mem. Soc. Astron. Ital.*, 54, 173
D’Antona F., Bellazzini M., Caloi V., Pecci F. F., Galletti S., Rood R., 2005, *ApJ*, 631, 868
D’Antona F., Vesperini E., D’Ercole A., Ventura P., Milone A., Marino A., Tailo M., 2016, *MNRAS*, 458, 2122
Da Costa G., 1981, in Proc. IAU Colloquium No. 68. Astrophysical Parameters for Globular Clusters. Kluwer, Dordrecht, p. 75
Decressin T., Meynet G., Charbonnel C., Prantzos N., Ekström S., 2007, *A&A*, 464, 1029

- Decressin T., Charbonnel C., Siess L., Palacios A., Meynet G., Georgy C., 2009, *A&A*, 505, 727
- Denisenkov P., Denisenkova S., 1989, *ATsir*, 1538, 11
- Denissenkov P. A., Hartwick F., 2013, *MNRAS*, 437, L21
- De Boer T. et al., 2012, *A&A*, 539, A103
- Frebel A., Norris J. E., Aoki W., Honda S., Bessell M. S., Takada-Hidai M., Beers T. C., Christlieb N., 2007, *ApJ*, 658, 534
- Gaia-Collaboration et al., 2018, *A&A*, 616, A1
- Geisler D., Smith V. V., Wallerstein G., Gonzalez G., Charbonnel C., 2005, *AJ*, 129, 1428
- Gratton R. et al., 2001a, *A&A*, 369, 87
- Gratton R. et al., 2001b, *A&A*, 369, 87
- Gratton R., Sneden C., Carretta E., 2004, *ARA&A*, 42, 385
- Harris W. E., 1996, *AJ*, 112, 1487
- Hasselquist S. et al., 2017, *ApJ*, 845, 162
- Hollyhead K. et al., 2016, *MNRAS*, 465, L39
- Hollyhead K. et al., 2018, *MNRAS*, 476, 114
- Hook I., Jørgensen I., Allington-Smith J., Davies R., Metcalfe N., Murowinski R., Crampton D., 2004, *PASP*, 116, 425
- Kirby E. N. et al., 2010, *ApJS*, 191, 352
- Kirby E. N. et al., 2015, *ApJ*, 801, 125
- Kirby E. N., Guhathakurta P., Bolte M., Sneden C., Geha M. C., 2009, *ApJ*, 705, 328
- Kraft R., 1994a, *PASP*, 106, 553
- Kraft R. P., 1994b, *PASP*, 106, 553
- Langer G., Hoffman R., Sneden C., 1993, *PASP*, 105, 301
- Lardo C. et al., 2016, *A&A*, 585, A70
- Lee J.-W., Carney B. W., Balachandran S. C., 2004, *AJ*, 128, 2388
- Lemasle B. et al., 2014, *A&A*, 572, A88
- Letarte B. et al., 2010, *A&A*, 523, A17
- Maeder A., Meynet G., 2006, *A&A*, 448, L37
- Majewski S., 2016, *Astron. Nachr.*, 337, 863
- Marino A. et al., 2014, *MNRAS*, 437, 1609
- Martell S. L., Smolinski J. P., Beers T. C., Grebel E. K., 2011, *A&A*, 534, A136
- McWilliam A., Wallerstein G., Mottini M., 2013, *ApJ*, 778, 149
- Milone A. et al., 2013, *ApJ*, 767, 120
- Milone A. et al., 2018, *MNRAS*, 481, 5098
- Norris J., 2004, *ApJ*, 612, L25
- Norris J., Freeman K., 1979, *ApJ*, 230, L179
- Norris J., Pilachowski C., 1985, *ApJ*, 299, 295
- Norris J., Cottrell P., Freeman K., Da Costa G., 1981, *ApJ*, 244, 205
- Norris J., Peterson B., Hartwick F., 1983, *ApJ*, 273, 450
- Norris J., Freeman K., Da Costa G., 1984, *ApJ*, 277, 615
- Norris J. E., Wyse R. F., Gilmore G., Yong D., Frebel A., Wilkinson M. I., Belokurov V., Zucker D. B., 2010, *ApJ*, 723, 1632
- Norris J. E., Christlieb N., Bessell M., Asplund M., Eriksson K., Korn A. J., 2012, *ApJ*, 753, 150
- Norris J. E., Yong D., Venn K. A., Gilmore G., Casagrande L., Dotter A., 2017, *ApJS*, 230, 28
- Osborn W., 1971, *Observatory*, 91, 223
- Pancino E., Rejkuba M., Zoccali M., Carrera R., 2010, *A&A Rev.*, 524
- Pietrzyński G. et al., 2008, *AJ*, 135, 1993
- Piotto G. et al., 2015, *AJ*, 149, 91
- Placco V. M., Frebel A., Beers T. C., Stancliffe R. J., 2014, *ApJ*, 797, 21
- Prantzos N., Charbonnel C., Iliadis C., 2007, *A&A*, 470, 179
- Pumo M., Siess L., Zappala R., 2008, preprint ([arXiv:0805.3611](https://arxiv.org/abs/0805.3611))
- Ramírez I., Meléndez J., 2005, *ApJ*, 626, 465
- Renzini A. et al., 2015, *MNRAS*, 454, 4197
- Salaris M., Weiss A., Ferguson J. W., Fusilier D. J., 2006, *ApJ*, 645, 1131
- Salgado C., Da Costa G., Yong D., Norris J., 2016, *MNRAS*, 463, 598
- Saunders W. et al., 2004, in *SPIE Astronomical Telescopes + Instrumentation*, SPIE, Bellingham, p. 389
- Schiavon R. P. et al., 2016a, *MNRAS*, 465, 501
- Schiavon R. P. et al., 2016b, *MNRAS*, 466, 1010
- Sharp R. et al., 2006, in *SPIE Astronomical Telescopes + Instrumentation*, SPIE, Bellingham, p. 62690G
- Shetrone M., Venn K. A., Tolstoy E., Primas F., Hill V., Kaufer A., 2003, *AJ*, 125, 684
- Shetrone M. D., Smith G. H., Stanford L. M., Siegel M. H., Bond H. E., 2013, *AJ*, 145, 123
- Smith G., Norris J., 1982, *ApJ*, 254, 149
- Smith G. H., Shetrone M. D., Bell R. A., Churchill C. W., Briley M. M., 1996, *AJ*, 112, 1511
- Smith G. H., Briley M. M., Harbeck D., 2005, *AJ*, 129, 1589
- Sneden C., 1973, *ApJ*, 184, 839
- Sneden C., Kraft R. P., Langer G., Prosser C. F., Shetrone M. D., 1994, *AJ*, 107, 1773
- Sobeck J. S. et al., 2011, *AJ*, 141, 175
- Stancliffe R. J., Church R. P., Angelou G. C., Lattanzio J. C., 2009, *MNRAS*, 396, 2313
- Starkenburger E. et al., 2010, *A&A*, 513, A34
- Suntzeff N., 1981, *ApJS*, 47, 1
- Tolstoy E., Irwin M. J., Cole A. A., Pasquini L., Gilmozzi R., Gallagher J., 2001, *MNRAS*, 327, 918
- Trefzger D., Langer G., Carbon D., Suntzeff N., Kraft R., 1983, *ApJ*, 266, 144
- Ventura P., D'Antona F., 2011, *MNRAS*, 410, 2760
- Ventura P., D'Antona F., Mazzitelli I., Gratton R., 2001, *ApJ*, 550, L65
- Walker M. G., Mateo M., Olszewski E. W., Gnedin O. Y., Wang X., Sen B., Woodroffe M., 2007, *ApJ*, 667, L53
- Walker M. G., Mateo M., Olszewski E. W., 2009a, *AJ*, 137, 3100
- Walker M. G., Mateo M., Olszewski E. W., Penarrubia J., Evans N. W., Gilmore G., 2009b, *ApJ*, 704, 1274
- Yong D., Grundahl F., Johnson J. A., Asplund M., 2008, *ApJ*, 684, 1159

This paper has been typeset from a $\text{\TeX}/\text{\LaTeX}$ file prepared by the author.